

The incidence of obscuration in active galactic nuclei

A. Merloni^{1*}, A. Bongiorno², M. Brusa^{1,3,4}, K. Iwasawa⁵, V. Mainieri⁶, B. Magnelli⁷, M. Salvato¹, S. Berta¹, N. Cappelluti⁴, A. Comastri⁴, F. Fiore², R. Gilli⁴, A. Koekemoer⁸, E. Le Floch⁹, E. Lusso¹⁰, D. Lutz¹, T. Miyaji^{11,12}, F. Pozzi³, L. Riguccini¹³, D.J. Rosario¹, J. Silverman¹⁴, M. Symeonidis^{15,16}, E. Treister¹⁷, C. Vignali³ and G. Zamorani⁴

¹Max-Planck-Institut für extraterrestrische Physik (MPE), Giessenbachstrasse 1, D-85748, Garching bei München, Germany

²INAF-Osservatorio Astronomico di Roma, Via di Frascati 33, 00040, Monteporzio Catone, Rome, Italy

³Dipartimento di Astronomia, Università di Bologna, Via Ranzani 1, 40127, Bologna, Italy

⁴INAF-Osservatorio Astronomico di Bologna, Via Ranzani 1, 40127, Bologna, Italy

⁵ICREA and Institut de Ciències del Cosmos (ICC), Universitat de Barcelona (IEEC-UB), Martí i Franquès, 1, 08028 Barcelona, Spain

⁶European Southern Observatory, K. Schwarzschildstr. 1, 85741, Garching, Germany

⁷Argelander-Institut für Astronomie, Universität Bonn, Auf dem Hügel 71, 53121 Bonn, Germany

⁸Space Telescope Science Institute, 3700 San Martin Drive, Baltimore MD 21218, U.S.A.

⁹Laboratoire AIM-Paris-Saclay, CEA/DSM/Irfu, CNRS, Université Paris Diderot, Saclay, pt courrier 131, 91191 Gif-sur-Yvette, France

¹⁰Max Planck Institute for Astronomy, Königstuhl 17, 69117 Heidelberg, Germany

¹¹Instituto de Astronomia, UNAM, Ensenada, Baja California, Mexico (PO Box 439027, San Diego, CA 92143-9027, USA)

¹²University of California, San Diego, Center for Astrophysics and Space Sciences, 9500 Gilman Drive, La Jolla, CA 92093-0424, USA

¹³NASA Ames, Moffett field, CA 94035, USA

¹⁴Kavli Institute for the Physics and Mathematics of the Universe, The University of Tokyo, 5-1-5 Kashiwanoha, Kashiwashi, Chiba, 277-8583, Japan

¹⁵University of Sussex, Department of Physics and Astronomy, Falmer, Brighton BN1 9QH, Sussex, UK

¹⁶Mullard Space Science Laboratory, University College London, Holmbury St. Mary, Dorking, Surrey RH5 6NT, UK

¹⁷Departamento de Astronomia, Universidad de Concepcion, Casilla 160-C, Concepcion, Chile

ABSTRACT

We study the incidence of nuclear obscuration on a complete sample of 1310 AGN selected on the basis of their rest-frame 2–10 keV X-ray flux from the XMM-COSMOS survey, in the redshift range $0.3 < z < 3.5$. We classify the AGN as obscured or un-obscured on the basis of either the optical spectral properties and the overall SED or the shape of the X-ray spectrum. The two classifications agree in about 70% of the objects, and the remaining 30% can be further subdivided into two distinct classes: at low luminosities X-ray un-obscured AGN do not always show signs of broad lines or blue/UV continuum emission in their optical spectra, most likely due to galaxy dilution effects; at high luminosities broad line AGN may have absorbed X-ray spectra, which hints at an increased incidence of small-scale (sub-parsec) dust-free obscuration. We confirm that the fraction of obscured AGN is a decreasing function of the intrinsic X-ray luminosity, while the incidence of absorption shows significant evolution only for the most luminous AGN, which appear to be more commonly obscured at higher redshift. We find no significant difference between the mean stellar masses and star formation rates of obscured and un-obscured AGN hosts. We conclude that the physical state of the medium responsible for obscuration in AGN is complex, and mainly determined by the radiation environment (nuclear luminosity) in a small region enclosed within the gravitational sphere of influence of the central black hole, but is largely insensitive to the wider scale galactic conditions.

Key words: Surveys, Catalogues, Galaxies:active, Galaxies: fundamental parameters, Galaxies: evolution

1 INTRODUCTION

The observational appearance of an Active Galactic Nucleus (AGN) is not only determined by its intrinsic emission properties, but also by the nature, amount, dynamical and kinematic state of

* E-mail: am@mpe.mpg.de (MPE)

any intervening material along the line of sight. Intrinsic obscuration does indeed play a fundamental role for our understanding of the overall properties of AGN. Large, systematic studies of their spectral energy distribution clearly show that the intrinsic shape of the X-ray continuum can be characterized by a power-law in the 2-10 keV energy range, with a relative narrow distribution of slopes: $\langle \Gamma \rangle = 1.8 \pm 0.2$ (Nandra & Pounds 1994; Steffen et al. 2006; Tozzi et al. 2006; Young et al. 2009). Thus, the hard slope of the Cosmic X-ray Background (CXRB) spectrum (well described by a power-law with photon index $\Gamma_{\text{CXRB}} \simeq 1.4$ at $E < 10$ keV), and the prominent peak observed at about 30 keV are best accounted for by assuming that the majority of active galactic nuclei are in fact obscured (Setti & Woltjer 1989; Comastri et al. 1995).

In the traditional ‘unification by orientation’ schemes, the baffling diversity of AGN observational classes is explained on the basis of the line-of-sight orientation with respect to the axis of rotational symmetry of the system (Antonucci & Miller 1985; Antonucci 1993; Urry & Padovani 1995). In particular, obscured and un-obscured AGN are postulated to be intrinsically the same objects, seen from different angles with respect to a dusty, large-scale, possibly clumpy, parsec-scale medium, which obscures the view of the inner engine (Elitzur 2008; Netzer 2008). According to the simplest interpretations of such unification schemes, there should not be any dependence of the obscured AGN fraction with intrinsic luminosity and/or redshift.

In recent years, new generations of synthesis models of the CXRB have been presented (Gilli et al. 2007; Treister et al. 2009; Akylas et al. 2012), following the publication of increasingly larger and deeper X-ray surveys, and reducing the uncertainties in the absorbing column density distribution. When combined with the observed X-ray luminosity functions, they now provide an almost complete census of Compton thin AGN (i.e., those obscured by columns $N_{\text{H}} < \sigma_{\text{T}}^{-1} \simeq 1.5 \times 10^{24} \text{ cm}^{-2}$, where σ_{T} is the Thomson cross section). This class of objects dominates the counts in the lower X-ray energy band, where almost the entire CXRB radiation has been resolved into individual sources (Worsley et al. 2005).

The results on the statistical properties of obscured AGN from these studies are at odds with the simple ‘unification-by-orientation’ scheme. In fact, evidence has been mounting over the years that the fraction of absorbed AGN, defined in different and often independent ways, appears to be lower at higher nuclear luminosities (Lawrence & Elvis 1982; Ueda et al. 2003; Steffen et al. 2003; Simpson 2005; Hasinger 2008; Brusa et al. 2010; Bongiorno et al. 2010; Burlon et al. 2011; Assef et al. 2013). Such an evidence, however, is not uncontroversial. As recently summarized by Lawrence & Elvis (2010, and references therein), the luminosity dependence of the obscured AGN fraction, so clearly detected, especially in X-ray selected samples, is less significant in other AGN samples, such as those selected on the basis of their extended, low frequency radio luminosity (Willott et al. 2000) or in mid-IR colors (Lacy et al. 2007). The reasons for these discrepancies are still unclear, with Mayo & Lawrence (2013) arguing for a systematic bias in the X-ray selection due to an incorrect treatment of complex, partially-covered AGN. In general, one would like to rely on large, complete samples selected on the basis of a robust tracer of bolometric luminosity (independently on the level of obscuration). Theoretically, hard X-ray and mid-IR selection should satisfy this basic requirement, with the former having the advantage of a much lower level of contamination by stellar processes (see e.g. Merloni & Heinz 2013, for a discussion).

Evidence for a redshift evolution of the obscured AGN fraction is even more controversial. Large samples of X-ray selected

objects have been used to corroborate claims of positive evolution of the fraction of obscured AGN with increasing redshift (La Franca et al. 2005; Treister et al. 2006; Hasinger 2008), as well as counter-claims of no significant evolution (Ueda et al. 2003; Tozzi et al. 2006; Gilli et al. 2007). More focused investigation on specific AGN sub-samples, such as $z > 3$ X-ray selected QSOs (Fiore et al. 2012; Vito et al. 2013), rest-frame hard X-ray selected AGN (Iwasawa et al. 2012), or Compton Thick AGN candidates (Brightman & Ueda 2012) in the CDFS have also suggested an increase of the incidence of nuclear obscuration towards high redshift. Of critical importance is the ability of disentangling luminosity and redshift effects in (collections of) flux-limited samples and the often complicated selection effects at high redshift, both in terms of source detection and identification/follow-up.

In a complementary approach to these ‘demographic’ studies (in which the incidence of obscuration and the covering fraction of the obscuring medium is gauged statistically on the basis of large populations), SED-based investigations look at the detailed spectral energy distribution of AGN, and at the IR-to-bolometric flux ratio in particular, to infer the covering factor of the obscuring medium in each individual source (Maiolino et al. 2007; Treister et al. 2008; Sazonov et al. 2012; Roseboom et al. 2013; Lusso et al. 2013). These studies also found general trends of decreasing covering factors with increasing nuclear (X-ray or bolometric) luminosity, and little evidence of any redshift evolution (Lusso et al. 2013). Still, the results of these SED-based investigations are not always in quantitative agreement with the demographic ones. This is probably due to the combined effects of the uncertain physical properties (optical depth, geometry and topology) of the obscuring medium (Granato & Danese 1994; Lusso et al. 2013), as well as the unaccounted for biases in the observed *distribution* of covering factors for AGN of any given redshift and luminosity (Roseboom et al. 2013).

Both the apparent decrease of the incidence of obscured AGN with intrinsic luminosity, as well as its possible redshift evolution, might be (and have been widely) considered an indirect signature of AGN feedback, in that powerful sources are able to clean up their immediate gaseous environments, responsible for the nuclear obscuration, more efficiently (see e.g. Archibald et al. 2002; Hopkins et al. 2006; Menci et al. 2008). In such AGN feedback models, unification-by-orientation scenarios are superseded by so-called ‘evolutionary’ ones, as the incidence of nuclear obscuration changes dramatically with time during the SMBH active phases. To account for this, different physical models for the obscuring torus have been proposed, all including some form of radiative coupling between the central AGN and the obscuring medium (e.g. Lawrence 1991; Maiolino et al. 2007; Nenkova et al. 2008).

Irrespective of any specific model, it is clear that a detailed physical assessment of the interplay between AGN fuelling, star formation and obscuration on the physical scales of the obscuring medium is crucial to our understanding of the mutual influence of stellar and black hole mass growth in galactic nuclei (Bianchi et al. 2012a). Conceptually, we can identify three distinct spatial regions in the nucleus of a galaxy on the basis of the physical properties of the AGN absorber. The outermost one is the gravitational sphere of influence of the supermassive black hole (SMBH) itself, also called Bondi Radius $R_{\text{B}} = 2GM_{\text{BH}}/\sigma^2 \simeq 10 M_{\text{BH},8} \sigma_{300} \text{ pc}$, where $M_{\text{BH},8}$ is the black hole mass in units of $10^8 M_{\odot}$, and σ_{300} can be either the velocity dispersion of stars for a purely collisionless nuclear environment, or the sound speed of the gas just outside R_{B} , measured in units of 300 km/s. To simplify, one can consider any absorbing gas on scales larger than the SMBH sphere of influence

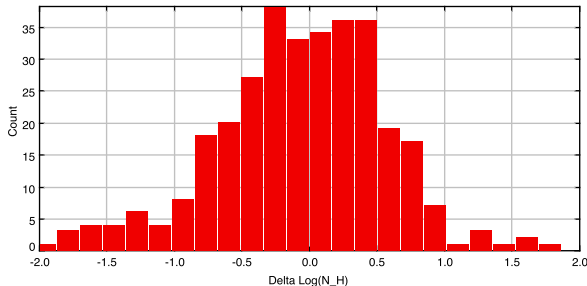


Figure 1. Distribution of the difference between the logarithm of the best fit absorption column density N_{H} (in cm^{-2}) between the HRz method and the full spectral analysis of Mainieri et al. (2011) for the 619 brightest sources in the sample.

to be “galactic”, in the sense that its properties are governed by star-formation and dynamical processes operating at the galactic scale. The fact that gas in the host galaxy can obscure AGN is not only predictable, but also clearly observed, either in individual objects (e.g. nucleus-obscuring dust lanes, Matt 2000), or in larger samples showing a lack of optically selected AGN in edge-on galaxies (Maiolino & Rieke 1995; Lagos et al. 2011). Indeed, if evolutionary scenarios are to supersede the standard unification by orientation scheme and obscured AGN truly represent a distinct phase in the evolution of a galaxy, then we expect a relationship between the AGN obscuration distribution and the larger scale physical properties of their host galaxies.

Within the gravitational sphere of influence of a SMBH, the most critical scale is the radius within which dust sublimates under the effect of the AGN irradiation. A general treatment of dust sublimation was presented in Barvainis (1987); Fritz et al. (2006), and subsequently applied to sophisticated clumpy torus models (Nenkova et al. 2008) or to interferometric observations of galactic nuclei in the near-IR (Kishimoto et al. 2007). For typical dust composition, the dust sublimation radius is expected to scale as $R_{\text{d}} \simeq 0.4 (L_{\text{bol},45}/10^{45})^{1/2} (T_{\text{sub}}/1500\text{K})^{-2.6}$ pc (Nenkova et al. 2008), as indeed confirmed by interferometry observations of sizable samples of both obscured and un-obscured AGN in the nearby Universe (Tristram et al. 2009; Kishimoto et al. 2011). Within this radius only atomic gas can survive, and reverberation mapping measurements do suggest that indeed the Broad emission Line Region (BLR) is located immediately inside R_{d} (Netzer & Laor 1993; Kaspi et al. 2005).

The parsec scale region between R_{d} and R_{B} is the traditional location of the obscuring torus of the classical unified model. On the other hand, matter within R_{d} may be dust free, but could still cause substantial obscuration of the inner tens of Schwarzschild radii of the accretion discs, where the bulk of the X-ray emission is produced (Dai et al. 2010; Chen et al. 2012). Indeed, a number of X-ray observations of AGN have revealed in recent years the evidence for gas absorption within the sublimation radius. Variable X-ray absorbers on short timescales are quite common (Risaliti et al. 2002; Elvis et al. 2004; Risaliti et al. 2007; Maiolino et al. 2010), and the variability timescales clearly suggests that these absorbing structures lie within (or are part of) the BLR itself.

In light of all this bewildering complexity, general interpretations and global models for the inner structure of a galaxy nucleus should be taken with extreme care, even very successful ones such as the ‘unification-by-orientation’ scheme. Issues of sample

selection, incompleteness, or incomplete coverage of the nuclear Spectral Energy Distribution (SED) should all be accounted for in order to properly assess the overall relevance, for the AGN population at large, of any observational trend.

Here we present a study of the obscuration properties of a very large sample of 1310 AGN selected in the XMM-COSMOS field (Hasinger et al. 2007) on the basis of their X-ray luminosity. In particular, we take advantage of the unprecedented level of identification and redshift completeness of the XMM-COSMOS (Brusa et al. 2010; Salvato et al. 2009, 2011) to perform a *rest-frame 2–10 keV* X-ray flux selection, thus mitigating the $N_{\text{H}}-z$ bias that plagues X-ray observed-frame flux limited samples (see e.g. Tozzi et al. 2006; Gilli et al. 2010a). The unique multi-wavelength coverage of the COSMOS field (Scoville et al. 2007) allows us to extract information on the host galaxies of the X-ray selected AGN. We rely on the SED decomposition method of Merloni et al. (2010) and Bongiorno et al. (2012) to derive robust stellar mass estimates for all objects in the sample, and use the FIR *Herschel-PEP* observations (Lutz et al. 2011) of the field to infer star-formation rate indicators. Finally, the extensive spectroscopic followup granted through the zCOSMOS (Lilly et al. 2007, 2009) and Magellan/IMACS (Trump et al. 2007, 2009) projects also plays a crucial role for the study we present here, together with archival data from the SDSS DR9 (Ahn et al. 2012).

The strength of our approach lies both in the sheer quantity and in the multi-wavelength quality of the data in hand. Not only are we able to explore the relationships among AGN obscuration, nuclear luminosity and host galaxy stellar mass in complete bins of the luminosity-redshift parameter space with high statistical accuracy, but we can also study the physical nature of the obscuration by comparing the classification of AGN into obscured and un-obscured based on different indicators (X-ray spectral analysis, optical spectroscopy, optical-NIR SED).

The structure of the paper is as follows. In section 2 we describe the sample and the selection process. In section 3 we explore the dependencies of the fraction of optically obscured AGN on luminosity, redshift and obscuration classification, while in section 4 we take a closer look at the relationship between obscured and un-obscured AGN and the stellar masses and star-formation rates of their hosts. Finally, in section 5 we examine critically differences and similarities in fraction of X-ray obscured AGN for the optical vs. the X-ray obscuration classification, before drawing our conclusions in section 6.

2 SAMPLE SELECTION

Our AGN were selected from the XMM-COSMOS point-like source catalog (Hasinger et al. 2007; Cappelluti et al. 2009), that includes ~ 1800 X-ray sources detected above a flux limit of $\sim 5 \times 10^{-16}$, $\sim 3 \times 10^{-15}$, and $\sim 7 \times 10^{-15}$ $\text{erg cm}^{-2} \text{s}^{-1}$ in the 0.5–2 keV, 2–10 keV, and 5–10 keV bands, respectively, and has been presented in Cappelluti et al. (2009), to which we also refer for a detailed discussion of the X-ray data analysis. Thanks to the rich multi-wavelength data in the field, almost complete reliable counterpart identification ($>98\%$) was achieved by Brusa et al. (2010); a combination of spectroscopic data (for more than half of the sources) and good-quality photometric redshifts (Salvato et al. 2009, 2011) ensures redshift completeness close to 100%.

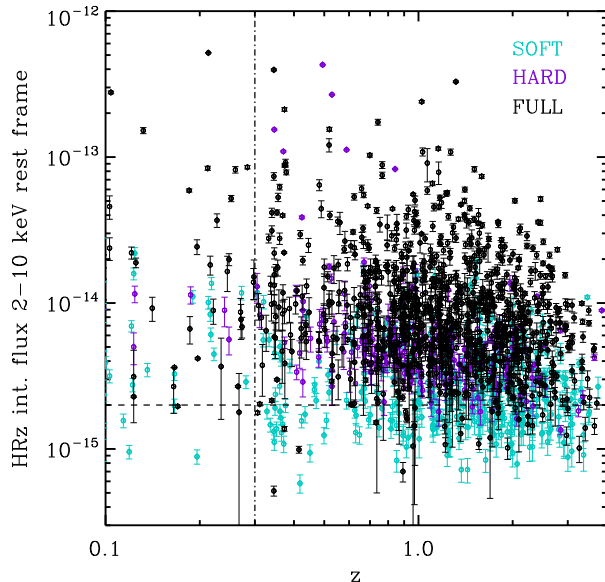


Figure 2. Intrinsic (absorption corrected) rest-frame 2-10 keV fluxes as a function of redshift for all the XMM-COSMOS AGN in the original sample. Black, cyan and purple circles denote objects detected in the full (0.5-2 and 2-10 bands), soft (0.5-2 keV) and hard (2-10 keV) bands, respectively. The dashed and dot-dashed lines mark our selection criteria for the analysis presented in this paper ($z > 0.3$ and $f_{2-10\text{keV,rest-frame}} = 2 \times 10^{-15}$).

2.1 Rest-frame flux selection and intrinsic luminosities

The main goal of this work is to study the incidence of obscuration in a large sample of X-ray selected AGN across a wide range of luminosity, host properties and, crucially, redshift. However, because of the wide energy band-pass of XMM, the X-ray selected sample described in the previous section is a mixture of objects that have been detected above the flux thresholds in the various energy bands. However, obscuration due to neutral gas affects different bands at different redshifts in different ways, causing a severe “obscuration-redshift” bias. As a result, flux-limited samples preferentially pick up more obscured objects at higher redshift (see e.g. Gilli et al. 2010a).

Fortunately, the AGN sample at our disposal allows us to circumvent (to a large extent) such a bias, as redshift is known for all sources in the sample: a simple K-correction of the observed spectrum can in principle guarantee a clean selection based on the *rest-frame* flux in any given band. In the following, we call this method for estimating rest-frame fluxes and luminosity on the basis of the observed hardness ratios (HR) and redshifts (z) the ‘HRz’ method (Ueda et al. 2003).

We proceed with the HRz in the following way. For the 619 brightest sources (those with more than 200 pn counts in the full 0.5-10 keV observed XMM band) we used the full spectral analysis of Mainieri et al. (2011), and obtain a value of the intrinsic column density N_{H} and rest-frame 2-10 keV flux (both observed and intrinsic). For all other sources, we compute the “observed” spectral slope (Γ_{obs}) that best reproduces the ratio of X-ray fluxes¹ in the soft (0.5–2 keV) and hard (2–10 keV) X-ray bands. For objects

¹ In each band, the fluxes had been derived from the observed counts using fixed conversion factors, as described in Cappelluti et al. (2009).

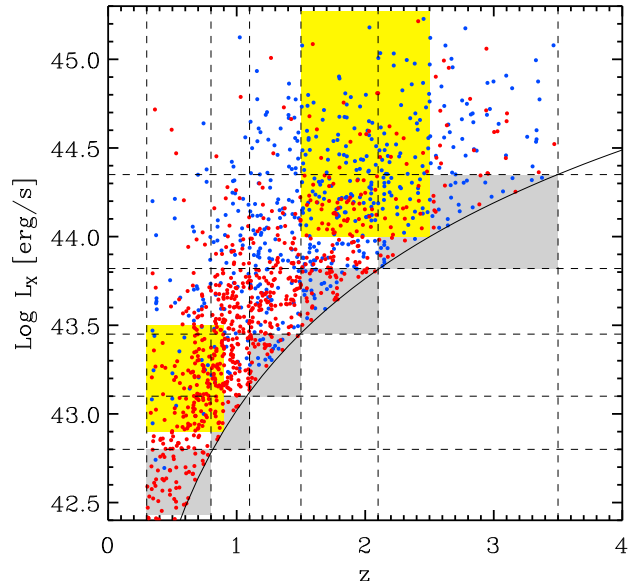


Figure 3. Intrinsic (absorption corrected) 2-10 keV luminosity-redshift plane distribution of the sources studied. Blue circles represent optically classified type-1 AGN, red ones type-2 AGN. The vertical and horizontal dashed lines show the binning adopted for subsequent studies of complete samples. The grey shaded area are incomplete bins, while the yellow regions define the two luminosity-redshift interval used to investigate the optical/X-ray misclassified AGN (see section 5.1 below).

detected only in one band, of course, we can only place an upper (if only a 2-10 keV detection is available) or a lower (if only a 0.5-2 keV detection is available) limit on the observed spectral slope. In these cases we assign each source a value of Γ_{obs} by picking from the tails of the observed distribution of spectral slopes among sources detected in both bands.

The intrinsic (absorption corrected) luminosity for the AGN in the sample was computed as in Brusa et al. (2010), i.e. on the basis of the full spectral analysis (see Mainieri et al. 2011), for objects with enough X-ray counts, while for the rest we use the HRz method to estimate a value of the absorbing column density $N_{\text{H,HRz}}$ in a statistical fashion, assuming each object has an intrinsic spectral slope which is normally distributed around a mean of $\Gamma_{\text{int}} = 1.8 \pm 0.2$ (1σ error)². The HRz method can be tested against full spectral analysis for the objects with the highest number of counts. The distribution of the difference in the logarithm of the best fit column densities is plotted in Figure 1. There are no apparent biases, although the scatter is substantial, but only slightly larger than the statistical uncertainty on the spectrally derived column densities, which has a median of about 0.3 dex.

The choice of a flux limit that defines our final sample is somewhat arbitrary, but has to be chosen on the basis of the best possible compromise between completeness and total number of sources in the sample. Figure 2 shows the rest-frame intrinsic 2-10 keV fluxes estimated with the HRz method as a function of redshift for the sources in the original sample. We chose to strike this compromise at $f_{2-10\text{keV,rest-frame}} = 2 \times 10^{-15}$ erg/s/cm², which is the intrinsic flux of the faintest sources detected in the hard band only

² All objects for which the inferred column density is smaller than an average galactic value of 3×10^{20} cm⁻² is assigned a value $\text{Log } N_{\text{H}} = 20$

(and thus most heavily obscured), further restricting our analysis to sources at $z > 0.3$, discarding only very few low-redshift genuine AGN. We tested the robustness of such a choice by applying more conservative flux limits, up to twice as bright a limit (i.e. up to 4×10^{-15} erg/s/cm²), but no qualitative change to the final results could be seen, apart from the obvious reduction of their statistical significance.

After excluding potential starburst galaxy contaminants (i.e. X-ray sources with 2-10 keV luminosity smaller than 2×10^{42} erg/s) we are left with a final sample of 1310 AGN selected on the basis of their intrinsic (absorption corrected) rest-frame 2-10 keV flux at $z > 0.3$.

We denote L_X the *intrinsic*, absorption-corrected 2-10 keV luminosity of the AGN. Because of the probabilistic way of assigning an intrinsic value for the spectral index to each source, our final rest-frame flux limited sample is statistical in nature: for the faint AGN detected in XMM-COSMOS, the individual values of L_X , N_H and Γ_{int} are not precisely known, but their ensemble average is accurate in a statistical sense. The sheer size of the sample then guarantees the robustness of our results. Figure 3 shows the distribution of the sources in the $L_X - z$ plane. In the following sections we will describe the main results of our analysis, performed in many instances by defining regions in the luminosity-redshift plane in which our sample is complete; incomplete bins in the $L_X - z$ plane are shaded in Figure 3.

One final note of caution is in place here. Such a simple approach for the absorption correction (i.e. the assumption that all objects can be corrected for by taking into account a uniform, full-covering, absorber) might be inadequate for more complex spectra, such as those produced by partial covering absorbers. These are known to be present in many local AGN (Winter et al. 2009), albeit at luminosities typically lower than those we are probing with our XMM-COSMOS sources. Such spectra are very hard to model properly in survey data with limited photon statistics (but see Brightman & Nandra 2012), but could dramatically affect our estimates of the sources' intrinsic luminosity, for objects with Compton Thick absorbers covering a high fraction of the sky seen by the X-ray emitter. If this kind of objects represents a non-negligible fraction of the overall AGN population, the resulting effects on the statistics of obscured AGN fraction can be profound, as demonstrated by Mayo & Lawrence (2013). This is not predicted by current synthesis models of the CXRB, which all imply very small fractions of CT AGN at the flux limits of XMM-COSMOS (see e.g. Akylas et al. 2012), but should obviously be checked with detailed spectral analysis of individual sources. Here, lacking the data quality sufficient for a proper treatment of partially-covered AGN, we compare the 2-10 keV intrinsic luminosity we derived with the mid-IR luminosity (rest frame $12\mu\text{m}$, measured from the overall optical/NIR SED fit, see Bongiorno et al. 2012).

Using a sample of local Seyfert galaxies (both Seyfert-1 and Seyfert-2) at high spatial resolution, Gandhi et al. (2009) found that the uncontaminated nuclear mid-IR continuum of AGN closely correlates with the intrinsic X-ray [2–10] keV AGN emitted powers over three orders of magnitude in luminosity, following the relation $\text{Log}(L_{\text{MIR}}/10^{43}) = (0.19 \pm 0.05) + (1.11 \pm 0.07)\text{Log}(L_X/10^{43})$. We show the $L_X - L_{\text{MIR}}$ for all the objects in our sample in Figure 5, color-coded by their absorption classification (see section 2.2 below). Our objects cluster closely along the Gandhi et al. relation, with a noticeable scatter. More importantly, only a handful of them have X-ray luminosities more than a factor of 10 smaller than what would be predicted on the basis of the $12\mu\text{m}$ luminosity. If our absorption corrections weren't accurate (as in the case in which most

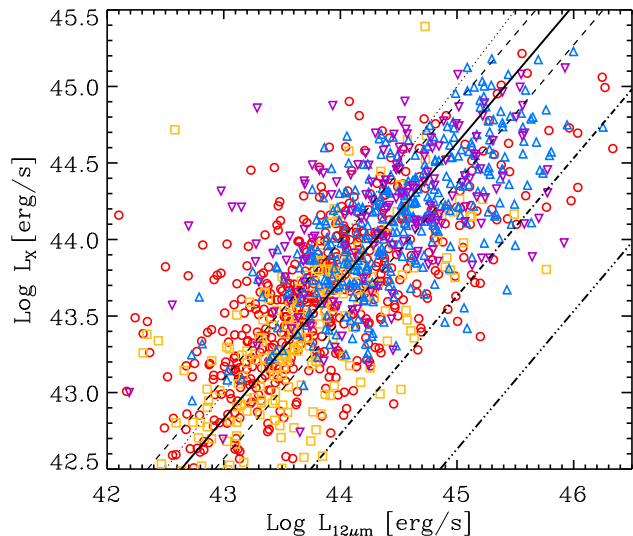


Figure 5. Intrinsic (absorption corrected) 2-10 keV X-ray luminosity vs. rest-frame $12\mu\text{m}$ luminosity (as derived from the optical/NIR SED fitting) for all AGN in the sample. Different colors and symbols represent objects with different optical and X-ray classification, as discussed in more detail in section 5 below. Red circles are for objects classified as obscured from both optical and X-ray spectra; blue upward triangles are un-obscured AGN from both optical and X-ray spectra; orange squares are optical type-2, but X-ray un-obscured, while purple downwards triangles are optical type-1, but X-ray obscured objects. The solid line is the best fit relation from Gandhi et al. (2009), with the dashed lines marking its $1-\sigma$ scatter. The dot-dashed and triple-dot-dashed lines mark the locus where X-ray luminosity is a factor of 10 and 100 lower than predicted by the Gandhi relation, respectively. The dotted line is the equality line, drawn to guide the eye only.

of the objects were buried, Compton Thick AGN), we would have observed much higher $L_{12\mu\text{m}}/L_X$ ratios. We conclude that, given the current limitations of the photon statistics, our simplified spectral analysis is justified. We cannot exclude that some objects might be affected by partial covering from a Compton Thick medium, but this should not qualitatively change the overall results we present below.

2.2 Obscuration classification and host galaxy properties

The sources in the final sample can be classified as obscured and un-obscured AGN according to their optical/NIR properties, as discussed in Brusa et al. (2010) and Bongiorno et al. (2012). First of all, for all the AGN with spectroscopic redshift information (742/1310 in our final sample), we classified as optically un-obscured (type-1) those (400) which show broad optical emission lines ($\text{FWHM} > 2000 \text{ km s}^{-1}$) and as optically obscured (type-2) all those (342) without broad emission lines. For the remaining 568 sources, for which only photometric redshifts are available, the source classification in type-1 and type-2 was performed on the basis of the template that best describes their SED as derived from Salvato et al. (2011); we have 130 “photometric” type-1 AGN and 438 “photometric” type-2. Photometric classification relies on observables such as point-like morphology in the HST/ACS images (Koekemoer et al. 2007), blue rest-frame optical/UV colors and significant variability to identify un-obscured AGN (Salvato et al. 2009; Lusso et al. 2010) (for more details, see the flowchart in figure 8 of Salvato et al 2011).

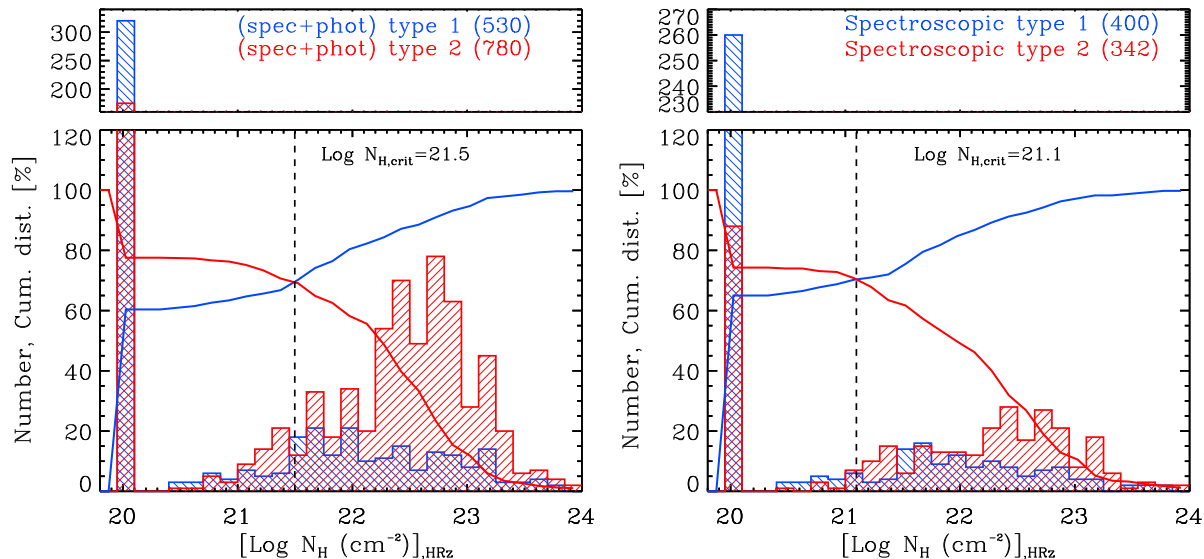


Figure 4. Distribution of the estimated column density (in logarithmic units) with the HRz method. Blue shaded histograms are for optically classified type-1 AGN, red ones for type-2. The *Left* panel is for the whole sample (spectroscopic and photometric; 1310 sources); the *Right* panel for the spectroscopic redshift sample (742 sources in total). In each panel the blue solid lines are the cumulative distribution $C(\text{Log}N_{\text{H}})$ (percentage) for the type-1 AGN, and the red solid line is $1 - C(\text{Log}N_{\text{H}})$ for the type-2. The vertical dashed lines indicates the values of $\text{Log}N_{\text{H}}$ that best separates the two samples.

As a first test of the different classification methods, we compare the column density estimated from the X-ray broad-band spectra (HRz method) with the optical classification in terms of type-1 and type-2 AGN described above. This is shown in Figure 4 both for the entire sample (left panel) and for the sub-sample of AGN with spectroscopic redshift information (right panel). As expected, type-1 AGN (optically un-obscured) have a column density distribution which is peaked at values consistent with little or no X-ray obscuration, but with a substantial tail at higher column densities. On the contrary, most type-2 (optically obscured) AGN appear to have column densities $\text{Log}N_{\text{H}} > 21$, but again with a non-negligible fraction of sources (both spectroscopically and photometrically classified) with X-ray spectra (or hardness ratios) consistent with no obscuration.

We can quantify this mismatch between the two classification methods (optical- and X-ray-based) by comparing the cumulative N_{H} distribution of the type-1 AGN (i.e. the cumulative number of objects with column density *smaller* than a given value, blue curves in Fig. 4) with the opposite of the cumulative N_{H} distribution of type-2 AGN (i.e. the cumulative number of objects with column density *larger* than a given value, red curves in Fig. 4). Their intersection tells us what value of N_{H} best separates the two samples (measured at $\text{Log}N_{\text{H}} = 21.5$ and $\text{Log}N_{\text{H}} = 21.1$ for the full and the spectroscopic samples, respectively), while the level at which the two curves intersect can be used to define a level of “coherence” of the two classifications, with unity being perfect consistency. As we can see from both panels, typically the two classifications agree to within about 70%, i.e. there are about 30% of optically classified type-1 (type-2) AGN with (without) evidence of absorption in the X-ray spectra. This is consistent with the similar analysis done by Trouille et al. (2009) on three separate *Chandra* survey fields. In the remaining of this work, we will adopt a value of $N_{\text{H,crit}} = 10^{21.5} \text{ cm}^{-2}$ to distinguish between X-ray obscured and un-obscured AGN. Similar values for the discriminating column density had been previously argued in studies of the optical prop-

erties of smaller hard X-rays selected samples (Della Ceca et al. 2008; Caccianiga et al. 2008).

It is worth noticing here that the values of the neutral hydrogen equivalent column density that best separate the obscured and un-obscured samples, providing the maximal overlap between the X-ray- and optical-based classification are smaller than the traditionally adopted value of 10^{22} cm^{-2} . Assuming a standard dust-to-gas ratio (Predehl & Schmitt 1995) and Galactic extinction law, the critical column densities correspond to optical extinction values of $E(B - V) \simeq 0.57$ for the entire sample and $E(B - V) \simeq 0.23$ for the spectroscopic sample. These values of extinction are consistent with the findings of Lusso et al. (2010), who have studied in detail the SED of spectroscopic type-1 AGN in COSMOS, concluding that only a negligible minority appears to suffer from reddening in excess of $E(B - V) = 0.2$.

Finally, we derive the host galaxy properties of our AGN using the results of the analysis presented in Bongiorno et al. (2012), where we introduced a procedure to fit the multi-wavelength SED of the sources by disentangling the nuclear and stellar contributions. In particular, as discussed in Bongiorno et al. (2012), at rest-frame wavelengths of about $1 \mu\text{m}$, three quarters of type-1 AGN have AGN fractions smaller than about 50%, implying that, even for un-obscured objects, our method allows a robust determination of the host total stellar masses, with typical uncertainty (statistical plus systematic) of the order of 0.4 dex (see also Merloni et al. 2010). Thanks to that approach, stellar masses for the host galaxies of all the AGN in our final sample could be obtained.

3 THE FRACTION OF OBSCURED AGN: LUMINOSITY, REDSHIFT AND CLASSIFICATION DEPENDENCIES

First of all, we examined the luminosity and redshift dependence of the fraction of AGN optically classified as obscured. The left hand panel of Figure 6 shows such a fraction as a function of in-

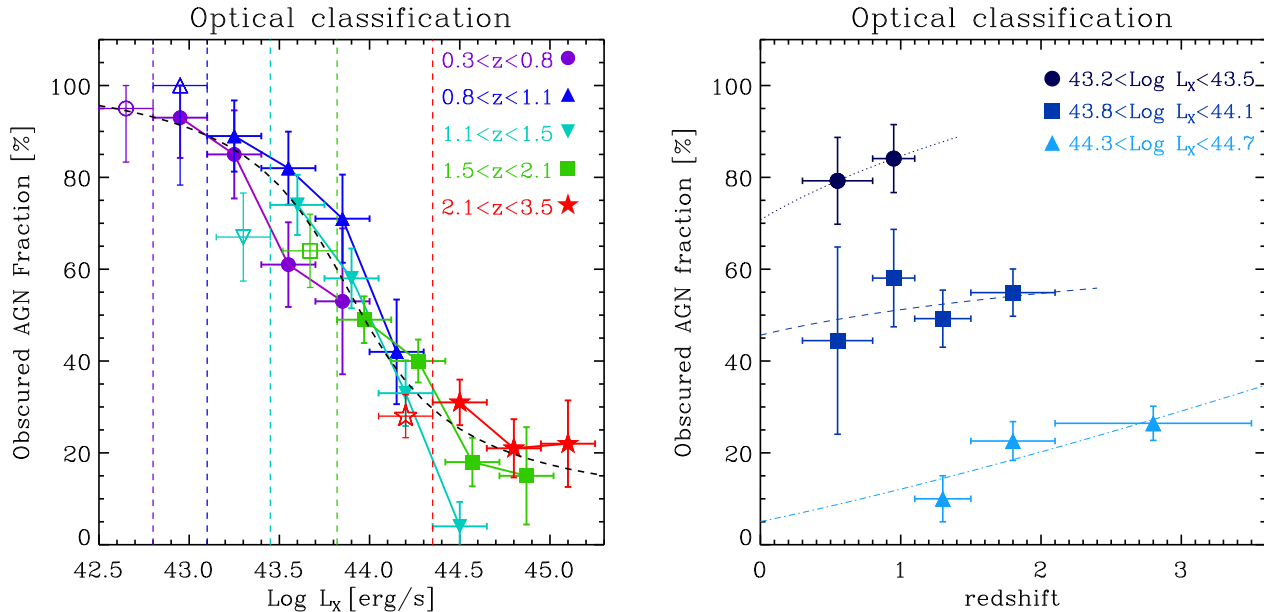


Figure 6. *Left Panel:* The fraction of optically obscured AGN is plotted versus the X-ray luminosity for different redshift bins (purple circles: $0.3 \leq z < 0.8$; blue upwards triangles: $0.8 \leq z < 1.1$; cyan downwards triangles: $1.1 \leq z < 1.5$; green squares: $1.5 \leq z < 2.1$ and red stars: $2.1 \leq z < 3.5$). The vertical dashed lines mark the luminosities above which the samples are complete in each redshift bin (of corresponding color). Empty symbols are from incomplete bins. The dashed line is the best fit to the entire data set across the whole redshift range (see text for details). *Right Panel:* Redshift evolution of the fraction of Obscured AGN in different luminosity bins (only those for which we are complete have been shown). The dotted, dashed, and dot-dashed lines show the best fit evolution in the three luminosity interval, respectively, according to Eq.(2). The best fit values for the parameter of each curve are reported in Table 2.

trinsic X-ray luminosity in five different redshift bins (see also Table 1). The decrease of the obscured AGN fraction with luminosity is strong, and confirms previous studies on the XMM-COSMOS AGN (Brusa et al. 2010). The dashed line, instead, shows the best fit relations to the optically obscured AGN fraction obtained combining all redshift bins. We assumed the relation to be of the form:

$$F_{\text{obs}} = A + \frac{1}{\pi} \text{atan} \left(\frac{l_0 - l_x}{\sigma_x} \right) \quad (1)$$

where $l_x = \text{Log} L_X$. The best-fit parameters we obtained are: $A = 0.56$; $l_0 = 43.89$ and $\sigma_x = 0.46$.

As mentioned before, the strong trend we observe could, at least partially, be due to an incorrect estimation of the intrinsic X-ray luminosity, which can induce an apparent trend of the obscured AGN fraction with luminosity, even in the absence of a real one. Mayo & Lawrence (2013) have shown that, in order for such an effect to be dominant, a substantial fraction (~ 50 - 60%) of all objects under study should be mis-modelled partially-covered AGN, with Compton Thick absorbers covering more than 95% of the X-ray source. This is difficult to rule out completely, but we note here that both the comparison with the estimated MIR luminosity, and the average X-ray spectral shape of the objects in our sample (see Figures 5 and 13) suggest that the fraction of Compton Thick AGN in the sample is not as large.

In section 2.2 we have shown how the classification based on the optical properties (spectroscopic and/or photometric) of the AGN and that based on the X-ray spectral analysis (mostly through the HRz method) agree in no more than 70% of the sample. Because of this, it is mandatory to explore and analyse the differences in the statistical properties of the sample when using an alternative (X-ray based) classification scheme. The left panel of Figure 7 shows the fraction of (X-ray classified) obscured AGN as a function

of intrinsic 2-10 keV X-ray luminosity (L_X) for different redshift intervals. Not in all redshift intervals there is a clear decrease of the fraction of obscured AGN with increasing luminosity; in particular, in the highest redshift bin the obscured AGN fraction remains almost constant, but the range of intrinsic luminosities sampled is too limited to draw firmer conclusions.

We now turn to a discussion of any possible evolutionary trend of the obscured AGN fractions as a function of redshift.

3.1 Redshift evolution

We plot in the right panels of Figures 6 and 7 the fraction of obscured AGN as a function of redshift, for three separate luminosity intervals and for the optical and X-ray classifications, respectively. Only bins where the sample is complete are shown. For optically classified AGN, we do not see any clear redshift evolution, apart from the highest luminosity objects (i.e. genuine QSOs in the XMM-COSMOS sample, with L_X between $10^{44.3}$ and $10^{44.7}$ erg/s). To better quantify this, we have fitted separately the evolution of the obscured fraction in the three luminosity bins with the function:

$$F_{\text{obs}} = B \times (1+z)^\delta. \quad (2)$$

The best fit parameters are shown in Table 2, while the best fit relations are shown as thin lines in the right panels of Figures 6 and 7. For the optical classification, as anticipated, we measure a significant evolution ($\delta_{\text{OPT}} > 0$) only for the most luminous objects, with $\delta_{\text{OPT}} = 1.27 \pm 0.62$. Previously, Treister & Urry (2006) had claimed a significant increase in the fraction of optically classified obscured AGN with redshift, on the basis of the analysis of a large sample extracted from a combination of seven different X-ray

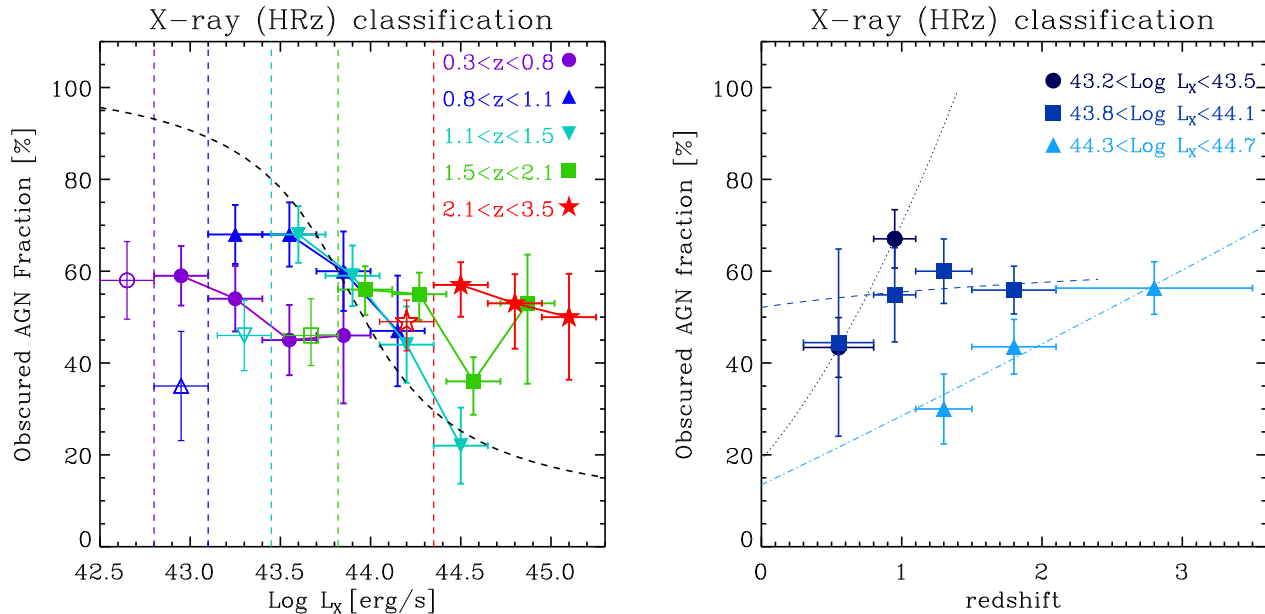


Figure 7. The fraction of X-ray obscured AGN is plotted versus the X-ray luminosity for different redshift bins (purple circles: $0.3 \leq z < 0.8$; blue upwards triangles: $0.8 \leq z < 1.1$; cyan downwards triangles: $1.1 \leq z < 1.5$; green squares: $1.5 \leq z < 2.1$ and red stars: $2.1 \leq z < 3.5$). The vertical dashed lines mark the luminosities above which the samples are complete in each redshift bin (of corresponding color). Empty symbols are from incomplete bins. The dashed line is here plotted as a reference, and represent the best fit to the absorbed AGN fraction vs. luminosity relation for optically obscured AGN, from Fig. 6 and Eq.(1). *Right Panel:* Redshift evolution of the fraction of Obscured AGN in different luminosity bins (only those for which we are complete have been shown). The dotted, dashed, and dot-dashed lines show the best fit evolution in the three luminosity interval, respectively, according to Eq.(2). The best fit values for the parameter of each curve are reported in Table 2.

surveys of various areas and depth. Their sample indeed covers a wider luminosity and redshift range, so is in principle better suited to disentangle their degeneracies, but, on the other hand, requires corrections to be made for compensating for the redshift incompleteness of the original X-ray selected sample, which could introduce biases, if the spectroscopic redshift completeness correlates with obscuration. Our nearly complete sample (within the volumes probed by the COSMOS field 2 deg^2 area), is at least minimally affected by such bias.

For the X-ray classification, we observe a significant evolution with redshift both at the lowest and highest luminosities, where the fraction of X-ray obscured AGN increases with z , consistent with previous findings by numerous authors (La Franca et al. 2005; Treister & Urry 2006; Hasinger 2008; Fiore et al. 2012; Vito et al. 2013). A more robust assessment of the redshift evolution of the obscured AGN fraction, however, would require a more extensive coverage of the $L - z$ plane than that afforded by our flux-limited XMM-COSMOS sample.

4 OBSCURED AGN AND GALAXY-WIDE PROPERTIES

4.1 Relationship between AGN obscuration and host galaxies stellar masses

An important test that is made possible by the quality of the data of the COSMOS AGN sample is to study whether the host galaxy stellar mass (M_*) plays any role in determining the statistics of (optically) obscured AGN in our sample. Figure 8 shows the distribution of the 1310 AGN in the sample in the $\text{Log } L_X - \text{Log } M_*$ plane. Most of the AGN hosts in our sample have stellar masses

within one decade (between $10^{10.3}$ and $10^{11.3}$ solar masses), but span a large range of “specific accretion rates” (Aird et al. 2012; Bongiorno et al. 2012), i.e. the observed ratio of nuclear X-ray luminosity to host galaxy stellar mass. Modulo the AGN bolometric correction, the standard scaling relation between M_* and the SMBH mass (Häring & Rix 2004) would imply that the specific accretion rate could be used as a rough proxy of the Eddington ratio, and Figure 8 shows that most AGN in our sample accrete at Eddington ratios of the order of 10%, but with a very wide distribution. The distribution of the host galaxies’ stellar masses for the two classes of AGN, with over-plotted the obscured AGN fraction (black circles with error bars) calculated for different mass bins is shown in the top panel of Figure 8. In each of these bins, the obscured AGN fraction is calculated mixing AGN of different luminosities, and the result is an almost mass-independent average obscured fraction of about 55%. It is interesting to note that a number of authors have previously noticed that the overall fraction of obscured AGN is a universal number, indeed close to this value (Lawrence & Elvis 2010). The difference with our findings could in part be due to the effect of applying very uncertain (and intrinsically scattered) bolometric corrections to a compilation of data-sets from different catalogs. The effect of this would be to wash out the true luminosity dependence and average the obscured AGN fraction to a value close to the sample mean of $\sim 55\%$. Alternatively, the problem could lie in the derivation of the intrinsic luminosity from the observed X-ray one, which could introduce a spurious luminosity dependence, as discussed in sections 2.1 and 3 above.

Despite its size, our sample is still too small to study simultaneously the obscured AGN fraction as a function of luminosity, redshift and stellar mass. However, the results of Fig. 6 indicate

Table 1. Fraction of optically (from figure 6) and X-ray (from figure 7) obscured AGN for various redshift and X-ray luminosity bins. Incomplete bins are marked with an asterisk.

$0.3 \leq z < 0.8$		
$\text{Log} L_X$ [erg/s]	Optical Obsc. Fract. [%]	X-ray Obsc. Fract. [%]
42.5 – 42.8	* 95^{+5}_{-12}	* 58 ± 8
42.8 – 43.1	93^{+7}_{-9}	59 ± 6
43.1 – 43.4	85 ± 10	54 ± 7
43.4 – 43.7	61 ± 9	45 ± 8
43.7 – 44.0	53 ± 16	46 ± 15
$0.8 \leq z < 1.1$		
$\text{Log} L_X$ [erg/s]	Optical Obsc. Fract. [%]	X-ray Obsc. Fract. [%]
42.8 – 43.1	* 100^{+0}_{-22}	* 35 ± 12
43.1 – 43.4	89 ± 8	68 ± 6
43.4 – 43.7	82 ± 8	68 ± 7
43.7 – 44.0	71 ± 10	60 ± 9
44.0 – 44.3	42 ± 11	47 ± 12
$1.1 \leq z < 1.5$		
$\text{Log} L_X$ [erg/s]	Optical Obsc. Fract. [%]	X-ray Obsc. Fract. [%]
43.15 – 43.45	* 67 ± 10	* 46 ± 8
43.45 – 43.75	74 ± 7	68 ± 6
43.75 – 44.05	58 ± 7	59 ± 7
44.05 – 44.35	33 ± 7	44 ± 8
44.35 – 44.65	4^{+5}_{-4}	22 ± 8
$1.5 \leq z < 2.1$		
$\text{Log} L_X$ [erg/s]	Optical Obsc. Fract. [%]	X-ray Obsc. Fract. [%]
43.52 – 43.82	* 64 ± 8	* 46 ± 7
43.82 – 44.12	49 ± 5	56 ± 6
44.12 – 44.42	40 ± 5	55 ± 6
44.42 – 44.72	18 ± 5	36 ± 7
44.72 – 45.02	15 ± 11	53 ± 17
$2.1 \leq z < 3.5$		
$\text{Log} L_X$ [erg/s]	Optical Obsc. Fract. [%]	X-ray Obsc. Fract. [%]
44.05 – 44.35	* 28 ± 5	* 49 ± 6
44.35 – 44.65	31 ± 5	57 ± 7
44.65 – 44.95	21 ± 6	53 ± 10
44.95 – 45.25	22 ± 9	50 ± 14

Table 2. Best fit parameter (from equation 2) for the redshift evolution of the obscured AGN in three different luminosity bins. The parameters for the optically classified AGN are marked by 'OPT', while those for the X-ray classified AGN by 'HRz'. In boldface, we highlight the sub-sample where significant redshift evolution is seen.

parameter	$\text{Log} L_X$ range		
	[43.2, 43.5]	[43.8, 44.1]	[44.3, 44.7]
B_{OPT}	0.71 ± 0.27	0.46 ± 0.20	0.05 ± 0.04
δ_{OPT}	0.26 ± 0.65	0.17 ± 0.46	1.27 ± 0.62
B_{HRz}	0.18 ± 0.09	0.52 ± 0.21	0.13 ± 0.07
δ_{HRz}	1.89 ± 0.77	0.09 ± 0.43	1.08 ± 0.42

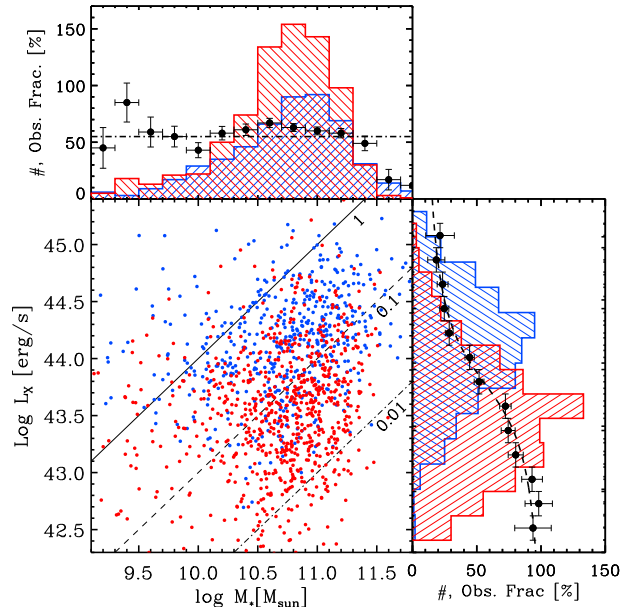


Figure 8. The main panel shows the distribution of the 1310 AGN in the $\text{Log} M_*$ - $\text{Log} L_X$ plane. Blue circles are optically classified type-1 objects, red type-2 objects. The dot-dashed, dashed, and solid lines mark the approximate locus of 1%, 10% and 100% of the Eddington limit, estimated by assuming constant 2-10 keV bolometric correction, κ_X and a universal M_{BH}/M_* ratio, such that $\kappa_X M_*/M_{\text{BH}} = 10^{3.9}$. The right hand panel shows the luminosity distributions for the two classes, with over-plotted the obscured AGN fraction (black circles with error bars) and the best fit relation of eq.(1). The top panel shows the distribution of the host galaxies' stellar masses for the two classes of AGN, with over-plotted the obscured AGN fraction (black circles with error bars) calculated for different mass bins; in each of these fixed stellar mass bins, the obscured AGN fraction is calculated mixing AGN of different luminosities, and the result is an almost mass-independent average obscured fraction of about 55% (dot-dashed horizontal line).

that, to a first approximation, redshift dependencies can be ignored for low- to moderate luminosity AGN. Therefore, we have carried out a study of the AGN fraction evolution as a function of intrinsic X-ray luminosity and host galaxy stellar mass across the entire redshift range spanned by our sample. The results are shown in the left panel of Figure 9. Clearly, the total stellar mass of the host galaxy does not appear to have any strong influence on the fraction of the optically obscured AGN in our sample, even if there is marginal evidence of a slightly larger fraction of obscured AGN in the most massive galaxies. The right hand panel of the same figure shows again the obscured AGN fraction for different stellar mass bins, but now plotted as a function of the specific accretion rate.

Not surprisingly, given what we discussed in section 3 and on the left panel of Fig. 9 itself, the specific accretion rate does not seem to be a good predictor of the obscured AGN fraction, and definitely it is a much worse one than the X-ray luminosity itself. Indeed, as shown by the dashed lines of the right panel of Fig. 9, the data are consistent with the simplest assumption that the fraction of (optically defined) type-2 AGN is *mainly* a function of luminosity, so that neither the Eddington ratio, not the overall gravitational potential of the host galaxy affects in a significant way the statistical properties of the optically obscuring medium.

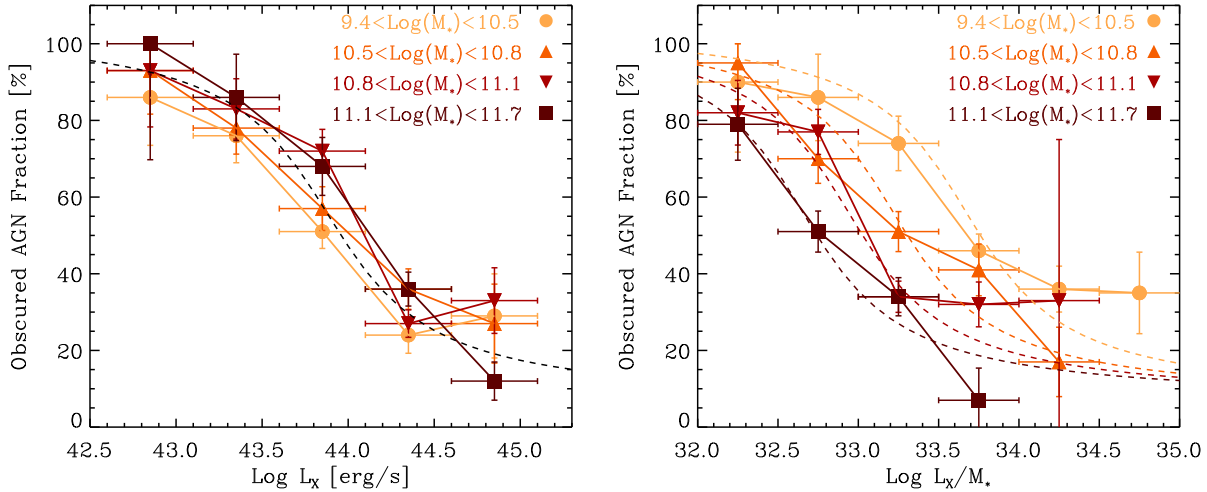


Figure 9. *Left:* The fraction of obscured AGN is plotted versus the X-ray luminosity for different host galaxy stellar mass bins. The dashed line is the best fit to the entire data set shown in Fig. 6. *Right:* The fraction of obscured AGN is plotted versus the specific accretion rate (L_X/M_*), for different host galaxy stellar mass bins. The dashed lines are the best fit of the to the entire data set shown in the left panel of Fig. 6, each shifted horizontally by the corresponding factor of $\text{Log} M_*$.

4.2 Relationship between AGN obscuration and host galaxies star formation

We have then analysed the relationship between AGN obscuration and the star-forming properties of their host galaxies. To avoid as much as possible the contaminating effects of the AGN itself for the determination of star-formation rate from optical-UV SED fitting, we have used the FIR data collected by *Herschel*/PACS (Poglitsch et al. 2010) guaranteed time, that has observed the entire COSMOS field as a part of the PEP-survey (Lutz et al. 2011, www.mpe.mpg.de/Research/PEP). Rosario et al. (2012) have studied in detail the possible influence of AGN-driven emission on the *Herschel*/PACS fluxes and stacks of X-ray selected sources in various deep fields. They concluded that AGN contamination is minimal, and affects only the objects with the lowest SFR. At the depth of the *Herschel*-PEP survey of the COSMOS field, however, only a relatively small fraction of the X-ray sources in our sample are individually detected ($\sim 18\%$). We thus resort to a stacking analysis to assess statistically the incidence of star formation in the host galaxies of our AGN.

In order to do so, we have stacked the *Herschel* fluxes, both at 100 and 160 μm , at the location of the detected counterparts of the AGN. We did so separately for objects classified as type-1 and type-2 in each of the 15 bins of the $L_X - z$ plane where our survey is complete (see Fig. 3). We define “detection” whenever the stacked signal exceeds a value of three times the noise in at least one PEP band in a bin. We then derive the SFR of each redshift, luminosity and obscuration-class bin using their stacked PACS flux densities and the Chary & Elbaz (2001) SED library. In the case where there are two PACS detections (at both 100 μm and 160 μm), we fit the PACS flux densities with the Chary & Elbaz (2001) SED library leaving the normalization of each template as a free parameter. If, on the other hand, the stacked flux is detected significantly in only one PACS band (either at 100 μm or 160 μm), the SFR is obtained simply using the scaled SED library. As it was shown by Elbaz et al. (2010, 2011), scaling the FIR templates to match a monochromatic luminosity provides robust (and non-degenerate)

estimates of the total FIR luminosity, and thus of the SFR. In both cases, SFR is given by integrating the best SED template from 8 to 1000 μm and using the standard relation between IR luminosity and star formation rate of Kennicutt (1998) for a Chabrier (2003) IMF. For bins where no stacked signal is detected, we derive robust upper limits for the average SFR.

The top panel of Figure 10 shows the average SFR for each of the 30 stacks we have considered, as a function of the average X-ray luminosity of the AGN that were included in the stacks. Different symbols distinguish type-1 (circles) from type-2 AGN (squares). The overall trend of the average star formation rate as a function of AGN X-ray luminosity mostly reflects the influence of distance on both quantities in our flux-limited sample. Within individual redshift intervals (points of the same color), there is little evidence of a correlation between L_X and $\langle SFR \rangle$, a result consistent with previous investigations of SFR in AGN hosts from *Herschel* survey data (Mullaney et al. 2012; Rosario et al. 2012). This might be due to the lack of any physical connection between SFR and accretion luminosity, or to the effect of rapid AGN variability modulating a long term correlation (Hickox et al. 2013).

Most striking, however, is the comparison between the average star formation rate of optically obscured and un-obscured AGN, shown in the bottom panel of Fig. 10. In fact, for essentially all bins in the luminosity-redshift plane for which we have at least one measure of the average SFR from the stacks, we see no difference whatsoever in the rate of star formation in type-1 and type-2 AGN, despite the wide range of luminosities probed. Clearly, galaxy-wide star formation does not appear to distinguish between type-1 and type-2 AGN, or, to put it differently, the physical entity responsible for the optical classification into obscured and un-obscured AGN is not strongly affected by the overall star-formation properties of the host galaxy.

Despite the intriguing differences in the AGN X-ray and optical classification, the main results presented in this section do not change qualitatively when we look at the host galaxies of AGN classified on the basis of their X-ray spectral properties. In the left panel of figure 11 we show the fraction of X-ray obscured AGN

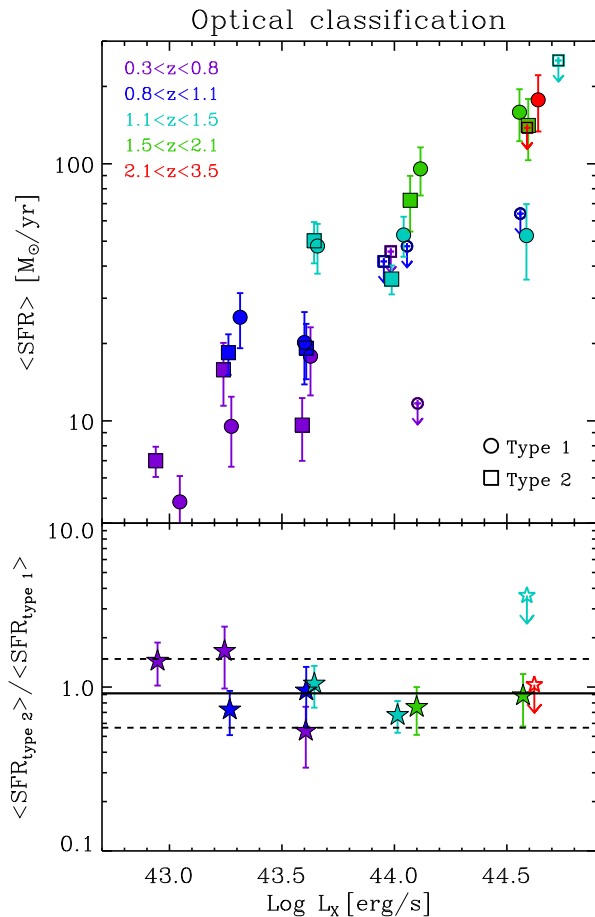


Figure 10. *Top Panel:* The mean star formation rates for AGN in different luminosity and redshift bins are plotted as a function of AGN X-ray luminosity. Different colors mark different redshift interval, with the same color-code of Fig. 6. Circles represent type-1 AGN and squares type-2 AGN. Empty symbols with downwards-pointing arrows mark upper limits. *Bottom Panel:* The ratio of the mean star formation rates in obscured (type-2) and un-obscured (type-1) AGN is plotted as a function of their X-ray luminosity. The solid line is the best fit mean value, with the uncertainty marked by the dashed lines.

as a function of stellar mass of their host galaxies. In order to improve the statistics, we restrict ourselves to the luminosity range $43.7 < \text{Log} L_X < 44.3$, where we can combine all objects within a wide redshift range ($0.3 < z < 2.1$), as the luminosity dependence is negligible there. Again, no strong dependence of the absorption fraction on M_* is evident. In the right hand panel of the same figure, we see that the average SFR computed from *Herschel-PEP* stacking analysis on the X-ray obscured and un-obscured AGN confirms our finding that the galaxy-wide SFR appears to be totally disconnected from the nuclear X-ray obscuring medium. This is consistent with the results of large *Herschel* studies over similar redshifts which find no clear dependence of SFR on X-ray obscuration (Shao et al. 2010; Rosario et al. 2012).

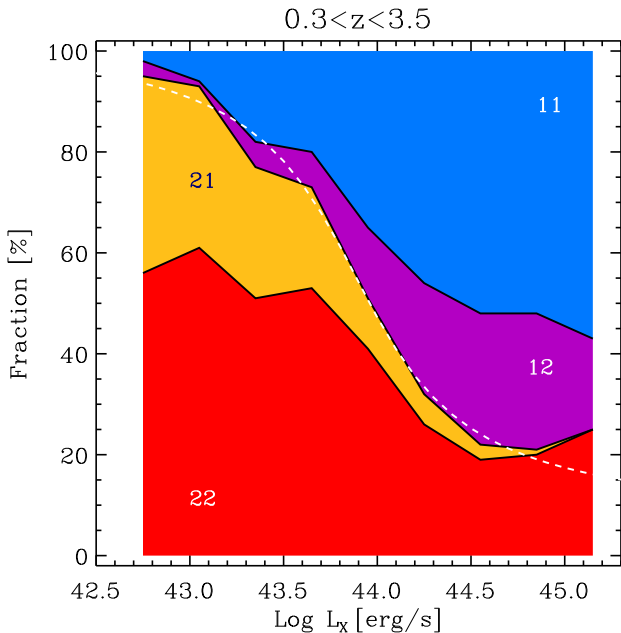


Figure 12. The relative fractions of AGN classified according to our 4-ways scheme are plotted as a function of intrinsic X-ray luminosity. Red shaded area is for type-22 AGN (both X-ray and optically obscured); blue for type-11 (both X-ray and optically un-obscured), while the orange shaded area is for type-21 objects (those which are X-ray un-obscured but optically obscured) and the purple one for type-12 AGN (optically un-obscured but X-ray obscured).

5 DISCUSSION: OPTICAL VS. X-RAY OBSCURATION CLASSIFICATION

As we showed in Section 3, the differences in the optical and X-ray based classification of the AGN are strongly luminosity dependent. We can show this if we introduce a 4-ways classification of the entire sample. Within such a scheme, we can define *type-11* AGN those which appear un-obscured both from their optical and X-ray spectra (363 in total); *type-22* objects are instead those which appear obscured both at X-ray and optical wavelengths (546). Finally, we call *type-12* AGN those which are optically un-obscured (showing broad lines in their optical spectra and/or a strong, blue optical/UV continuum and a point-like morphology) but have X-ray spectra (or hardness ratios) consistent with a value of $N_H > 10^{21.5} \text{ cm}^{-2}$ (167); conversely we call *type-21* those which are consistent with no X-ray obscuration, but does not show broad lines in their optical spectra, or have galaxy-like optical/UV Spectral Energy Distributions (234).

Figure 12 shows the distribution of these four classes as a function of luminosity (across the entire redshift range spanned by our sample). The $\sim 30\%$ AGN with ambiguous classification clearly separate into two distinct luminosity regimes: type-21 (orange shaded area) at low- and type-12 (purple shaded area) at high luminosities. We now discuss in greater detail the properties of these classes of objects.

5.1 Clues on the nature of the optical/X-rays discrepant classification: stacked spectra

The two sets of AGN with discordant classification call for a physical explanation. Having shown that this is most likely not to be

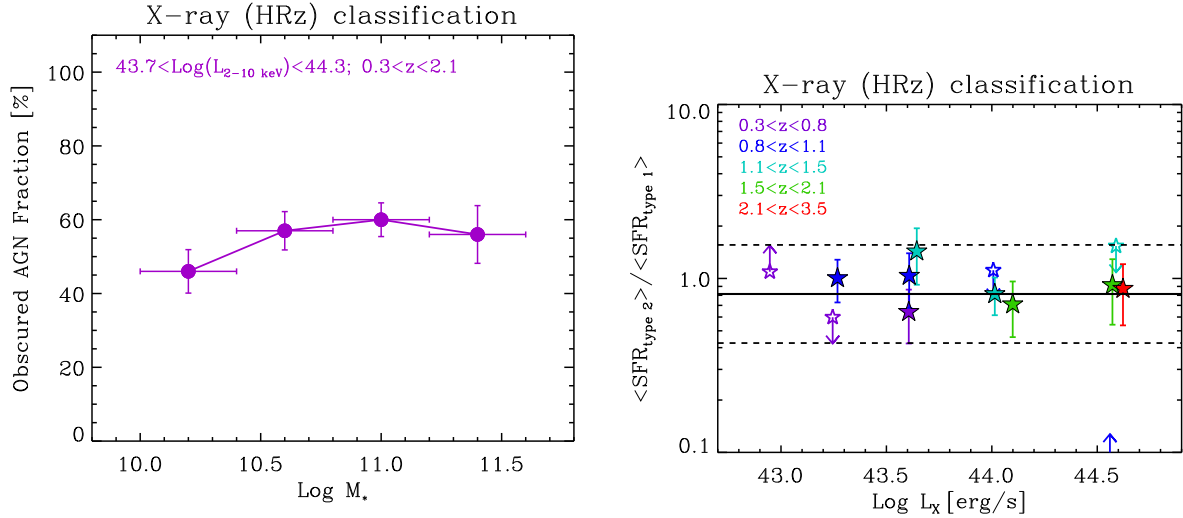


Figure 11. *Left:* Fraction of obscured AGN, as classified from their X-ray spectra with the HRz method, as a function of their host galaxies stellar mass, for all AGN in the sample with $43.7 < \text{Log} L_X < 44.3$ and $0.3 < z < 2.1$. *Right:* The ratio of the mean star formation rates in HRz classified as obscured (type-2) and un-obscured (type-1) AGN is plotted as a function of their X-ray luminosity. The solid line is the best fit mean value, with the uncertainty marked by the dashed lines.

searched in a different property of the host galaxies, we need to investigate in more detail the properties of the nuclear emission on parsec and sub-parsec scales, where the X-ray and optical features (big blue bump and/or broad lines) used to classify the objects are produced.

First, we have looked at the average spectral shape of four separate groups of objects. As we discussed before, there are two clearly separate regimes we need to study. At low luminosities (and, in our flux-limited sample, at low redshift) many X-ray un-obscured AGN are optically classified as obscured (type-21 class). In order to sample this regime, we took a complete sample, selected in the redshift range $0.3 < z < 0.9$ and with $42.9 < \text{Log} L_X < 43.5$ (see the leftmost yellow area in Fig. 3), and constructed the average X-ray and optical spectra for the type-21 (57 objects, 47 of which with spectroscopic redshift information) and type-22 AGN (99 objects, 61 with spec-z), respectively. On the other hand, in order to study the properties of the high-luminosity AGN that are classified as obscured from the HRz method, but appear optically un-obscured, we took a complete sample, selected in the redshift range $1.5 < z < 2.5$ and with $\text{Log} L_X > 44$ (rightmost yellow area in Fig. 3), and constructed the average X-ray and optical spectra for the type-11 (109 objects, 94 with spectroscopic redshifts) and type-12 AGN (66 objects, 38 with spec-z), respectively.

For the X-ray rest-frame spectral stacking, we adopt the method of Iwasawa et al. (2012), and produce rest-frame stacked spectra in the 2-10 keV range using the *XMM-Newton* data, and the four rest-frame stacked X-ray spectra are shown in Figure 13. We also compared the optical properties of the samples by stacking all available optical spectra. For this latter exercise, as we combine spectroscopic observations with different instruments (SDSS, IMACS, VLT/VIMOS from the zCOSMOS bright and deep surveys), covering different wavelength ranges at different resolutions, we first smooth all spectra to the resolution of the worst spectrum available (set at $R=300$ by the zCOSMOS deep program for the high redshift type-11 and type-12 samples and at $R=600$ by the zCOSMOS bright spectra for the low redshift type-21 and type-22 samples), then normalize at a common rest-frame wavelength (2200 Å for the type-11 and type-12 at high redshift, and 4500 Å

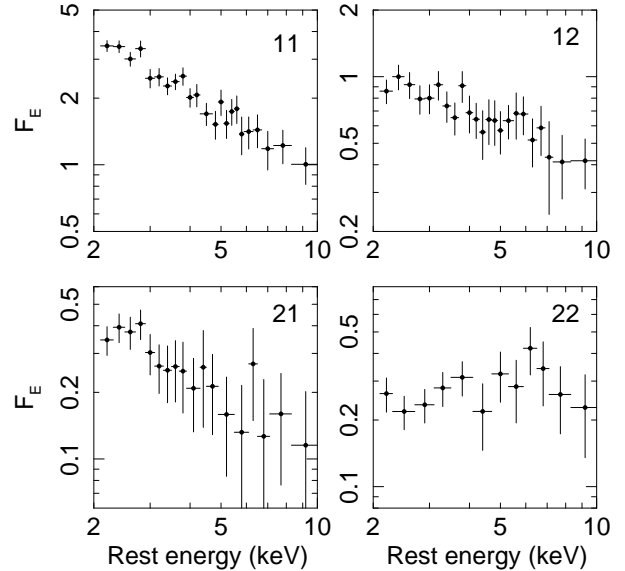


Figure 13. Rest frame stacked X-ray spectra for the four classes of objects in two different regions of the $L_X - z$ plane (see yellow boxes in Fig. 3 and section 5.1). The top row shows the stacked spectra for type-11 and type-12 AGN, respectively, in the $1.5 < z < 2.5$ redshift range and with $L_X > 10^{44}$ erg/s. The bottom row shows the stacked spectra for type-21 and type-22 AGN, respectively, in the $0.3 < z < 0.9$ redshift range and with $10^{42.9} < L_X < 10^{43.5}$ erg/s.

for the type-21 and type-22 at low redshift) and finally compute the mean rest-frame spectrum.

5.1.1 The most luminous AGN: closing in on the close-in absorber

The top row of Figure 13 shows the two stacked X-ray spectra for the two high-redshift, high-luminosity groups: type-11 (up-

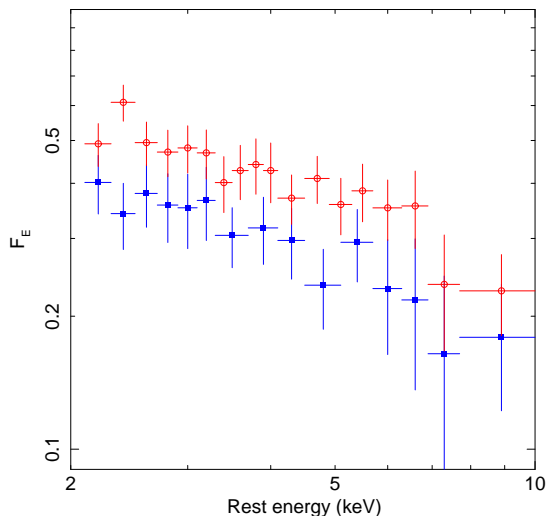


Figure 14. Rest frame stacked X-ray spectra for type-12 AGN with spectroscopic redshift information (red points) and with photo-z (blue points). The spectroscopic sample is the same used to produce the median optical spectrum shown with a purple line in Fig. 15 below. Both samples can be described by a simple power-law model fit with spectral index ~ 1.5 , or with an absorbed power-law model of $\Gamma_{12} \simeq 1.7$ and $N_{\text{H}} \simeq 7 \times 10^{21} \text{ cm}^2$.

per left) and type-12 (upper right). As expected, all luminous AGN classified as un-obscured from both X-ray and optical analysis show an almost featureless power-law spectrum, with slope $\Gamma_{11} = 1.9 \pm 0.1$, consistent with the basic assumption of the HRz method. No clear evidence of emission lines is seen, possibly consistent with the so-called Iwasawa-Taniguchi effect, i.e. the observational fact that the equivalent width of the ubiquitous narrow Fe K α emission line decreases with increasing X-ray luminosity for the AGN (Iwasawa & Taniguchi 1993; Bianchi et al. 2007; Chaudhary et al. 2010). The average rest-frame X-ray spectrum of the type-12 AGN has a significantly shallower slope: when fitted with a simple power-law, we obtain $\Gamma_{12} = 1.5 \pm 0.1$. However, an equally good fit can be obtained with an absorbed power-law model with $\Gamma_{12} \simeq 1.7$ and $N_{\text{H}} \simeq 7 \times 10^{21} \text{ cm}^{-2}$, suggesting that indeed there could be excess absorption in these optically classified, highly luminous, type-1 AGN. Note that the difference between type-11 and type-12 median X-ray spectra cannot be due to the 28 type-12 objects without spectroscopic information, as type-12 objects with and without spectroscopic redshift show almost identical rest-frame stacked X-ray spectra, as can be seen in Figure 14.

Incidentally, the fact that no significant iron emission line is detected in these two stacked spectra can be used to argue against a large fraction of these sources being hidden behind a Compton Thick screen with high covering fraction, as required by the model of Mayo & Lawrence (2013) to explain the observed obscured fraction vs. luminosity relation.

The left hand panel of Figure 15 shows the comparison between the rest-frame median optical spectra of type-11 and type-12 AGN. The spectroscopic completeness of the two samples is significantly different: while the template spectrum for the type-11 AGN is made with 71/109 object in the complete X-ray selected sample, we have only 31/66 spectra for the type-12. Nevertheless, the stacked optical spectra of the two classes are very similar, with no clear evidence that the type-12 are more reddened than the type-11, and no significant discrepancy in the equivalent width of the most prominent broad emission lines. Moreover, the median SED derived by stacking the best fit models of all photometric observa-

tions for type-11 and type-12 AGN in this redshift and luminosity range do not show any substantial difference either, as can be seen in the left panel of Figure 16. This suggests that large-scale (or galaxy-wide) extinction is not the cause of the X-ray obscuration, and contradicts the naive expectation of AGN evolutionary models in which powerful, obscured QSOs are associated to galactic absorption produced by the vigorous star-formation activity. While the most luminous AGN in our sample tend to be hosted by galaxies with high star-formation rate, there is no evidence of any relationship between this and the obscuration properties of the sources (see Figure 10 and 11).

In fact, it seems more plausible to argue that the excess X-ray obscuration in a large fraction of the most luminous AGN could be produced by dust-free gas within (or inside) the broad line region. In the nearby Universe, the presence of small-scale (sub-parsec) absorbers has been inferred in a number of cases (Risaliti et al. 2002; Maiolino et al. 2010), with NGC 4151 being the prototypical example, well known since more than thirty years (Ives et al. 1976). Evidence of excess absorption in more luminous, distant Type-1 QSOs was already highlighted by Perola et al. (2004), Fiore et al. (2012) and, for AGN in the *Chandra*-COSMOS survey, by Lanzuisi et al. (2013). An interesting possibility, worth further exploration, is that type-12 AGN might be related to Broad absorption-line quasars (BALQSOs). BALQOs have indeed long been known to be X-ray obscured (see e.g. Green et al. 1995; Gallagher et al. 1999; Brandt et al. 2000), even if more recent works on X-ray selected samples questioned this evidence (Giustini et al. 2008). Due to the lack of a systematic analysis of the optical spectra of broad-line AGN in the zCOSMOS and IMACS spectroscopic surveys and the inclusion of photometric type 1 AGN, we do not have a robust estimate of the BAL fraction in our sample. Assuming they constitute about 10-15% of the entire quasar population (Richards et al. 2003; Hewett & Foltz 2003), BALQSOs may be numerous among type-12 AGN. Indeed, a tantalizing hint of extra absorption can be seen in the stacked spectrum of type-12 AGN in Figure 15.

5.1.2 The nature of Type-21 AGN at low luminosity

Let us now consider the opposite end of the luminosity scale: among lower luminosity AGN (with $L_{\text{X}} < 10^{44} \text{ erg/s}$), a substantial fraction (about 1/3) is optically classified as type-2, but is un-obscured in the X-rays, and we called these objects type-21 AGN. These might well include so-called 'true' type-2 AGN (Panessa & Bassani 2002; Brightman & Nandra 2008; Bianchi et al. 2012b), i.e. accreting black holes without a hidden broad line region. Our sample of 234 such objects is about one order of magnitude larger than any previous one.

In the local Universe, objects of this class had been identified among Seyfert 2 galaxies by the lack of polarized broad emission lines (Tran 2001, 2003), and a number of theoretical investigations have explored models for the BLR and/or for the obscuring torus which naturally account for their disappearance at lower luminosities (Nicastro 2000; Nenkova et al. 2008; Elitzur & Ho 2009), even if in most models this effect sets in at much lower luminosities and/or Eddington ratios than those probed by our sample. We cannot discard this as a viable interpretation of our data, but we note that the concurrent effect of galaxy dilution, i.e. the decreasing contrast between the nuclear AGN emission and the stellar light from the whole galaxy must play an important role, too.

A simple estimate illustrates this point (see e.g. Merloni & Heinz 2013). Let us consider an AGN with optical B-band luminosity given by $L_{\text{AGN,B}} = \lambda L_{\text{Edd}} f_{\text{B}}$, where we

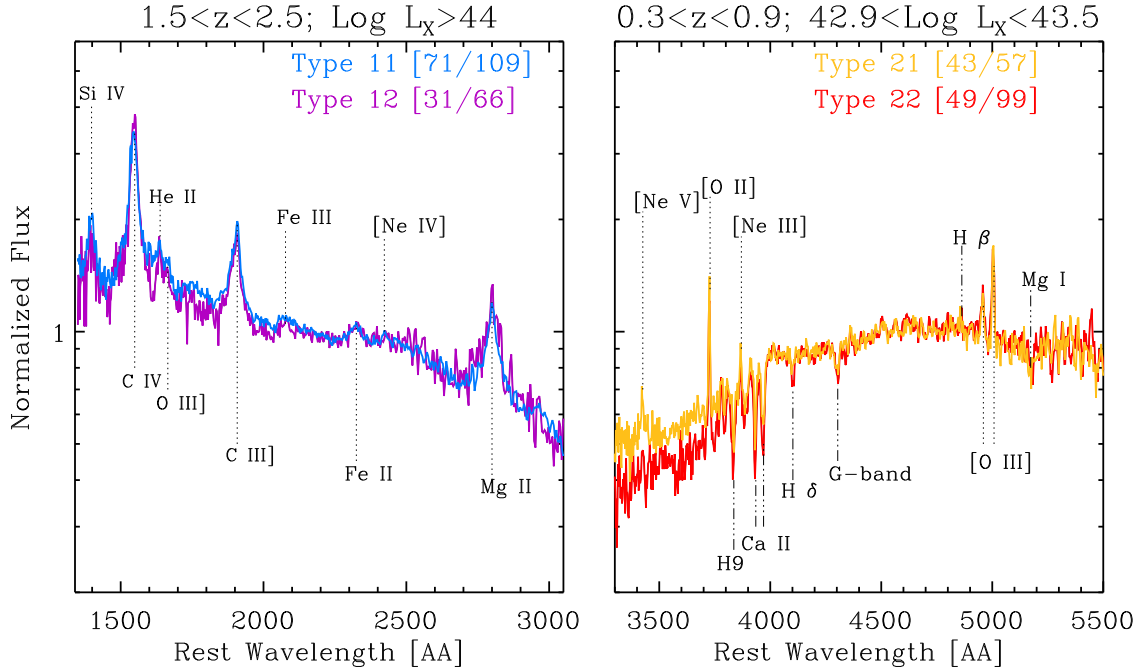


Figure 15. *Left:* Rest frame median spectra for the two high-redshift, high-luminosity classes of objects, type-11 and type-12, are plotted with blue and purple lines, respectively. The most prominent emission lines are marked. Spectra are normalized at 2200 Å. *Right:* Rest frame median spectra for the two low-redshift, low-luminosity classes of objects, type-21 and type-22, are plotted with orange and red lines, respectively. The most prominent emission and absorption lines are marked. Spectra are normalized at 4500 Å.

have introduced the Eddington ratio ($\lambda \equiv L_{\text{bol}}/L_{\text{Edd}}$)³, and a bolometric correction $f_B \equiv L_{\text{AGN,B}}/L_{\text{bol}} \approx 0.1$ (Richards et al. 2006). Assuming a bulge-to-black hole mass ratio of 0.001 and a bulge-to-total galactic stellar mass ratio of (B/T) , the contrast between nuclear AGN continuum and host galaxy blue light is given by:

$$\frac{L_{\text{AGN,B}}}{L_{\text{host,B}}} = \frac{\lambda}{0.1} \frac{(M_*/L_B)_{\text{host}}}{3(M_\odot/L_\odot)} (B/T) \quad (3)$$

Thus, for typical mass-to-light ratios, the AGN will become increasingly diluted by the host stellar light in the UV-optical-IR bands at Eddington ratios λ smaller than a few per cent, which is quite common among lower luminosity type-2 AGN in the sample (see Figure 8).

Broadly speaking, in order to understand the nature of type-21 AGN, three explanations can be put forward (see e.g. Bianchi et al. 2012b), depending on how much do the X-ray spectra reveal the true un-absorbed nature of these objects: (i) low-luminosity AGN do not produce broad lines, as the physical conditions in the accretion disc and its associated outflows are not favorable for the generation of a broad-line region (Nicastro 2000; Elitzur & Ho 2009); (ii) these weak type-1 AGN are simply out-shined by the stellar light from the massive host galaxy they live in, especially at the relative longer wavelengths probed by the majority of spectrographs used to follow-up XMM-COSMOS AGN in this luminosity range, and (iii) these objects are indeed heavily obscured (Compton Thick, CT), and the soft X-ray spectra appear because of a strong scattered

continuum (Brightman & Nandra 2012; Mayo & Lawrence 2013). NGC 1068 (Pier et al. 1994) would be the prototypical analog in the nearby Universe.

In the first case we expect no difference whatsoever between the optical/NIR SED of objects with obscured or un-obscured X-ray spectra, while in the second case a weak nuclear continuum should emerge at shorter wavelengths. In the CT case, the optical spectra of type-22 and type-21 should be similar, but the type-21 should have a much stronger hot dust component in the NIR.

The bottom row of Fig. 13 shows the two X-ray spectra for the two low-redshift, low-luminosity groups: type-21 (lower left) and type-22 (lower right). The type-22 AGN show a clear signature of obscured spectra, with an apparent curvature, and an overall shape that, if fitted with a simple power-law, would require a very hard slope $\Gamma_{22} = 0.8 \pm 0.2$. On the other hand, the vast majority of AGN which are HRz-classified as un-obscured in the type-21 class must indeed not show any evidence of cold, neutral absorption: the stacked X-ray spectrum, despite the low signal to noise, can be fitted with a power-law of slope $\Gamma_{21} = 1.8 \pm 0.2$. A tantalizing excess consistent with emission from Iron $K\alpha$ at 6.4 is apparent (with Equivalent Width ~ 300 eV), but significant at just the 2σ level; where this the telltale of heavily obscured AGN (which have typically EW of the order of 1 keV), one could speculate that a fraction of the order of 20% of the type-21 AGN could harbour heavily obscured nuclei.

Still, for the majority of the type-21 classification the fundamental question we need to answer is: why do the optical spectra of these low-luminosity AGN, the X-ray spectra of which are by and large un-obscured, not show any evidence of un-obscured AGN emission?

³ $L_{\text{Edd}} = 4\pi GM_{\text{BH}}m_p c/\sigma_T \simeq 1.3 \times 10^{38} (M_{\text{BH}}/M_\odot) \text{ ergs s}^{-1}$ is the Eddington luminosity

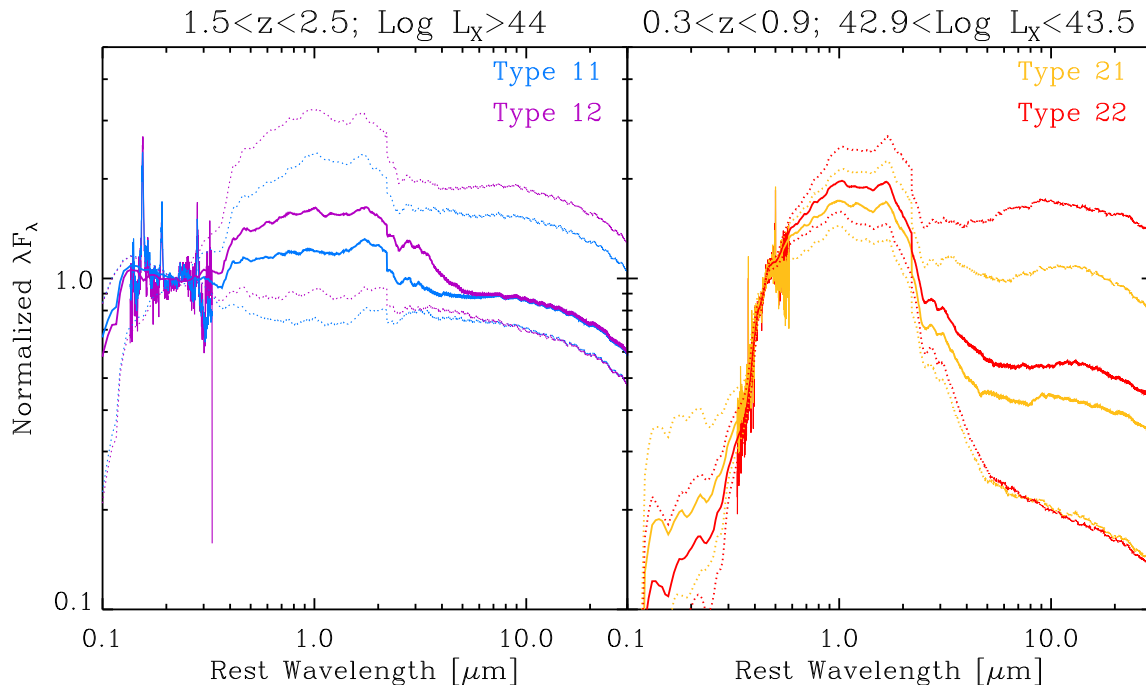


Figure 16. *Left:* Rest-frame median SED for type-11 and type-12 AGN (blue and purple solid lines, respectively). The dashed lines mark the 25th and 75th percentiles. The median spectra for the spectroscopic samples, all normalized at the same rest-frame wavelength (2200 Å) are over-plotted. *Right:* Rest-frame median SED for type-21 and type-22 AGN (orange and red solid lines, respectively). The dashed lines mark the 25th and 75th percentiles. The median spectra for the spectroscopic samples, all normalized at the same rest-frame wavelength (4500 Å) are also over-plotted. In both panel, and for all four AGN groups, we note a substantial agreement between the SED of the complete samples, and of the spectroscopic ones.

To further examine this issue, we show in the right hand panel of Figure 15 the comparison between the rest-frame median spectra of type-21 and type-22 AGN. As opposed to the case of the type-11 and type-12 median spectra, we see now two clearly galaxy-dominated spectra, displaying a strong stellar continuum with superimposed absorption features seen typically in massive galaxies. Also the global SED derived from combining the best-fit models to the entire photometric data-sets, shown in the right panel of Figure 16, are dominated by the host-galaxy stellar emission all the way to the rest-frame NIR. Within the wavelength range where the signal-to-noise of the stacked spectrum is high enough, no strong broad emission line can be seen (the only one expected being $H\beta$), neither in the type-22 AGN, nor in the type-21 AGN composite. However, two differences can be seen between the two composites: the type-21 spectrum has significantly stronger continuum blueward of the 4000 Å break, and a prominent, clearly visible [Ne V] $\lambda 3426$ emission line, that could be the signature of the optical/UV ionizing continuum emerging from the redder host galaxy stellar light (Gilli et al. 2010b; Mignoli et al. 2013). In fact, the emergence of a blue continuum shortwards of the 4000 Å break could suggest that, for the majority of type-21 AGN, galaxy dilution is the most plausible explanation. This is also confirmed by the measured ratio between mid-IR (rest frame $12\mu\text{m}$, measured from the overall SED fit, see Bongiorno et al. 2012) and intrinsic 2-10 keV luminosity, which we plot in Figure 17 for the four relevant subclasses (type-11 and type-12 in the top panel; type-21 and type-22 in the bottom one).

Finally, we show in Figure 17, that the $L_{12\mu\text{m}}/L_X$ ratio is similarly distributed in type-21 and type-22 objects, and, as shown

already in Fig. 5, consistent with the expected ratio for a pure, unobscured AGN, based on the best-fit relation of Gandhi et al. (2009) (solid vertical line). Thus, if the MIR luminosity is dominated by the AGN (as we assumed in our SED modelling, see Bongiorno et al. 2012), then our absorption correction to the X-ray luminosity must be by and large correct, as we discussed in section 2.1.

Further detailed studies of individual type-21 sources will be necessary to resolve the conundrum, including rest-frame UV and NIR spectroscopy, polarization and radio observations.

6 CONCLUSIONS

In this work, we have looked in great detail at the obscuration properties of a complete sample of AGN selected by *XMM-Newton* in the COSMOS field. The unique multi-wavelength coverage of the 2 deg^2 of the XMM-COSMOS area allows a full identification of the X-ray sources counterparts, and an extraordinary redshift completeness, by means of both spectroscopic observations and well-calibrated photometric redshift analysis. This, in turn, enables us to perform a basic K-correction of the X-ray spectra for all objects for which the number of X-ray counts is insufficient for a thorough spectral analysis. We could therefore select a large (1310 AGN) sub-sample of the XMM-COSMOS AGN above a fixed rest-frame 2-10 keV intrinsic flux (equal to $2 \times 10^{-15}\text{ erg/s/cm}^2$), in the redshift range $0.3 < z < 3.5$, conveniently mitigating the bias caused by the degeneracy between redshift and neutral absorption column density.

We classify *all* the AGN in our sample as obscured or un-

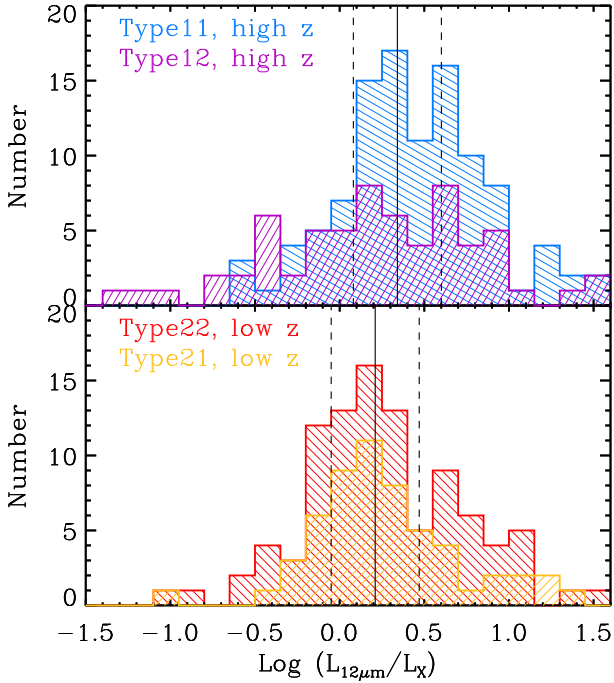


Figure 17. Distribution of the ratio between MIR (rest-frame $12\mu\text{m}$) and intrinsic X-ray luminosities for the four selected sub-samples discussed in the text. The top panel shows type–11 and type–12 AGN in the high-redshift, high-luminosity range, while the bottom shows the type–21 and type–22 AGN in the low-luminosity, low-redshift range. The vertical solid line mark the expected ratio (at the corresponding luminosity) for un-obscured, un-contaminated AGN from the relation of Gandhi et al. (2009), with the dashed lines denoting $1\text{-}\sigma$ uncertainty. This is an indirect confirmation that our absorption correction to the X-ray luminosity is, statistically, correct, as therefore should be our HRz classification.

obscured on the basis of either (i) the optical spectral properties and/or the overall spectral energy distribution and optical morphology or (ii) the shape of the X-ray spectrum.

To our knowledge, this is the largest systematic study of the difference between type–1 and type–2 AGN classifications based on X-ray vs. optical spectral energy distributions (see e.g. Corral et al. 2011; Malizia et al. 2012, for a comparison). Our ability to provide optical and X-ray classifications for a large, completely identified sample of X-ray selected AGN uncovers the complexity of the obscuring medium in the nuclear region of active galaxies. Our main conclusions are the following:

- By contrasting the cumulative distribution of the inferred column density for optically obscured and un-obscured AGN, we found that the most consistent classification divide occurs at $\text{Log } N_{\text{H}} \simeq 21.5$, corresponding to an optical reddening of $E(B - V) = 0.57$, for standard dust-to-gas ratio. This is not too surprising, as already above $E(B - V) \approx 0.3$ the optical ($0.3 - 1\mu\text{m}$) slope of a typical QSO would become red (Bongiorno et al. 2012; Hao et al. 2013). Nevertheless, such ‘optimized’ classification still fails for about 30% of the entire sample, for which the optical- and X-ray-based classifications give contrasting results. These ‘unclassifiable’ AGN clearly separate into two well distinct classes according to their nuclear luminosity (or redshift: in our flux-limited sample we are not able to fully disentangle these two possibilities).

- By studying the stacked X-ray and optical spectra of both the low-luminosity, low-redshift type–21 AGN we conclude that their optical classification as obscured, despite the apparently un-obscured X-ray spectra, is most likely due to host galaxy dilution, even if we cannot rule out that a small minority of these objects are CT AGN or true ‘naked’ type–2.

- The high-luminosity, high-redshift type–12 objects, instead, appear to be truly X-ray obscured, despite their optical SED typical of type–1 QSOs, and we argue that such excess absorption could be produced by dust-free gas within (or inside) the broad line region.

- The simplest version of the classical ‘unification by orientation’ scheme needs to be modified to account for the strong luminosity-dependence of the obscured AGN fraction. Radiative coupling between the central AGN and the source of obscuration must be the critical ingredient of any model, with the physics of dust sublimation probably playing a fundamental role. We cannot completely rule out the possibility that a substantial fraction of the AGN in our sample have more complex spectra than what we have assumed. If they are in fact dominated by almost complete covering from Compton Thick material, this could, at least partially, contribute to artificially enhance the dependence of the obscured AGN fraction on luminosity. The discrepancy in the literature between the statistics of obscured AGN fractions in X-ray, optical, radio and mid-IR selected samples (Lawrence & Elvis 2010) warrants further exploration of this issue. Here we simply note that, for the bulk of our sample, the IR-to-X-rays luminosity ratio is consistent with the values of a local sample observed at high angular resolution (Gandhi et al. 2009), suggesting that our estimated intrinsic X-ray luminosities are not biased low.

- As far as the redshift evolution of the obscured AGN fraction is concerned, we clearly do not detect any significant evolution in the optically obscured AGN fraction at low-to-moderate luminosities (see the right panels of figures 6 and 7), while obscured AGN (both X-ray and optically classified) at high luminosity are more common at high redshift. Hasinger (2008) had compiled a similarly sized sample of AGN from a number of different surveys, and studied the evolution of the obscured fraction, defined in a hybrid way (from optical spectra, when available, and from X-ray hardness ratio otherwise). He found an increase with redshift of the fraction of obscured AGN, but, as remarked by Gilli et al. (2010a), the lack of a proper K-correction in Hasinger (2008) induces a severe redshift- N_{H} bias (see our discussion in section 2 above), whereby an intrinsically constant fraction of obscured AGN as a function of redshift would have shown strong positive evolution. Having corrected for such an effect, albeit in a rudimentary way, due to the poor photon statistics for most of our sources, we can conclude that the most significant redshift evolution is displayed only by the most luminous AGN.

- All measurable host galaxy properties in our sample do not show any relationship with the obscured/un-obscured classification. Stellar masses can be measured quite accurately for the XMM-COSMOS AGN, as previously demonstrated by Merloni et al. (2010) and Bongiorno et al. (2012), and shown by the characteristic shape of the 4000 \AA break in the median SED of all four exemplary classes of AGN we discussed in section 5.1. When controlling for the redshift and/or the luminosity of the sources, we do not see any dependence of the obscured fraction on the host galaxy stellar mass (Figure 9 and 11).

- Even more striking is the lack of any significant difference between the average star-formation rate of obscured and un-obscured AGN, as probed by the stacked *Herschel* fluxes at the position of the sources in the sample (Figure 10). This is remarkable, as the sam-

ple spans a wide range of redshift, nuclear luminosity, and average SFR. In Bongiorno et al. (2012) we have measured indirectly the AGN duty cycle by measuring the fraction of AGN in a complete parent sample of field galaxies as a function of nuclear luminosity, host stellar mass and specific accretion rate. There we found a universal functional form that describes the probability of a galaxy to host an AGN as a function of the specific accretion rate, the normalization of which increases with redshift in steps with the increase of the specific star-formation rate. This led to the suggestion that, in a statistical sense, AGN activity and star formation may be globally correlated, but that there is little physical connection in each individual source between the gas accreting onto the SMBH and the material out of which stars form throughout the galaxy. Here we confirm this general view, by demonstrating the lack of any connection between the matter obscuring the accreting black holes (on pc or sub-pc scales) and the galaxy-wide SFR, consistent with the conclusions of large comprehensive Herschel studies (Rosario et al. 2012).

In closing, we note that, despite the large size of the complete sample of X-ray selected AGN studied here, we are still limited by small number statistics once we attempt to unravel the true nature of the relations between obscuration (N_{H}), luminosity, redshift, host galaxy stellar mass and star-formation rate. Arguably, only the next generation of massive AGN surveys enabled by the *eROSITA* all-sky X-ray survey (Merloni et al. 2012; Kolodzig et al. 2013), with its expected harvest of hundreds of thousands of AGN, will enable the necessary leap forward, provided extensive multi-wavelength coverage can be obtained over very wide areas of the sky.

ACKNOWLEDGMENTS

We thank K. Nandra, M. Brightman, J. Buchner, M. Elitzur for useful discussions, and the referee, Andy Lawrence, for his insightful comments and suggestions. AM and MS acknowledge financial support from the DFG cluster of excellence “Origin and structure of the universe” (www.universe-cluster.de). AB is supported by the INAF fellowship program. KI thanks support from Spanish Ministerio de Ciencia e Innovación (MICINN) through the grant AYA2010-21782-C03-01. AC acknowledges financial contribution from the agreement ASI-INAF I/009/10/0 and INAF-PRIN 2011. The HST COSMOS Treasury program was supported through NASA grant HST-GO-09822. This work is mainly based on observations obtained with *XMM-Newton*, an ESA Science Mission with instruments and contributions directly funded by ESA Member States and the USA (NASA), and with the European Southern Observatory under Large Program 175.A-0839, Chile. In Germany, the *XMM-Newton* project is supported by the Bundesministerium für Wirtschaft und Technologie/Deutsches Zentrum für Luft und Raumfahrt (BMWi/DLR, FKZ 50 OX 0001), the Max-Planck Society, and the Heidenhain-Stiftung. Herschel is an ESA space observatory with science instruments provided by European-led Principal Investigator consortia and with important participation from NASA. PACS has been developed by a consortium of institutes led by MPE (Germany) and including UVIE (Austria); KU Leuven, CSL, IMEC (Belgium); CEA, LAM (France); MPIA (Germany); INAF-IFSI/OAA/OAP/OAT, LENS, SISSA (Italy); IAC (Spain). This development has been supported by the funding agencies BMVIT (Austria), ESA-PRODEX (Belgium), CEA/CNES (France), DLR (Germany), ASI-INAF (Italy), and CICYT/MCYT (Spain). We acknowledge the use of the TOP-CAT software (<http://www.starlink.ac.uk/topcat/>).

We gratefully acknowledge the contribution of the entire COSMOS collaboration; more information on the COSMOS survey is available at <http://www.astro.caltech.edu/cosmos>.

REFERENCES

- Ahn C. P. et al., 2012, *ApJS*, 203, 21
 Aird J. et al., 2012, *ApJ*, 746, 90
 Akylas A., Georgakakis A., Georgantopoulos I., Brightman M., Nandra K., 2012, *A&A*, 546, A98
 Antonucci R., 1993, *ARAA*, 31, 473
 Antonucci R. R. J., Miller J. S., 1985, *ApJ*, 297, 621
 Archibald E. N., Dunlop J. S., Jimenez R., Friaça A. C. S., McLure R. J., Hughes D. H., 2002, *MNRAS*, 336, 353
 Assef R. J. et al., 2013, *ApJ*, 772, 26
 Barvainis R., 1987, *ApJ*, 320, 537
 Bianchi S., Guainazzi M., Matt G., Fonseca Bonilla N., 2007, *A&A*, 467, L19
 Bianchi S., Maiolino R., Risaliti G., 2012a, *Advances in Astronomy*, 2012
 Bianchi S. et al., 2012b, *MNRAS*, 426, 3225
 Bongiorno A. et al., 2012, *MNRAS*, 427, 3103
 Bongiorno A. et al., 2010, *A&A*, 510, A260000+
 Brandt W. N., Laor A., Wills B. J., 2000, *ApJ*, 528, 637
 Brightman M., Nandra K., 2008, *MNRAS*, 390, 1241
 Brightman M., Nandra K., 2012, *MNRAS*, 422, 1166
 Brightman M., Ueda Y., 2012, *MNRAS*, 423, 702
 Brusa M. et al., 2010, *ApJ*, 716, 348
 Burlon D., Ajello M., Greiner J., Comastri A., Merloni A., Gehrels N., 2011, *ApJ*, 728, 58
 Caccianiga A. et al., 2008, *A&A*, 477, 735
 Cappelluti N. et al., 2009, *A&A*, 497, 635
 Chabrier G., 2003, *PASP*, 115, 763
 Chary R., Elbaz D., 2001, *ApJ*, 556, 562
 Chaudhary P., Brusa M., Hasinger G., Merloni A., Comastri A., 2010, *A&A*, 518, A58
 Chen B., Dai X., Kochanek C. S., Chartas G., Blackburne J. A., Morgan C. W., 2012, *ApJ*, 755, 24
 Comastri A., Setti G., Zamorani G., Hasinger G., 1995, *A&A*, 296, 1
 Corral A., Della Ceca R., Caccianiga A., Severgnini P., Brunner H., Carrera F. J., Page M. J., Schwope A. D., 2011, *A&A*, 530, A42
 Dai X., Kochanek C. S., Chartas G., Kozłowski S., Morgan C. W., Garmire G., Agol E., 2010, *ApJ*, 709, 278
 Della Ceca R. et al., 2008, *A&A*, 487, 119
 Elbaz D. et al., 2011, *A&A*, 533, A119
 Elbaz D. et al., 2010, *A&A*, 518, L29
 Elitzur M., 2008, *New Ast. Rev.*, 52, 274
 Elitzur M., Ho L. C., 2009, *ApJL*, 701, L91
 Elvis M., Risaliti G., Nicastro F., Miller J. M., Fiore F., Puccetti S., 2004, *ApJL*, 615, L25
 Fiore F. et al., 2012, *A&A*, 537, A16
 Fritz J., Franceschini A., Hatziminaoglou E., 2006, *MNRAS*, 366, 767
 Gallagher S. C., Brandt W. N., Sambruna R. M., Mathur S., Yamasaki N., 1999, *ApJ*, 519, 549
 Gandhi P., Horst H., Smette A., Hönig S., Comastri A., Gilli R., Vignali C., Duschl W., 2009, *A&A*, 502, 457
 Gilli R., Comastri A., Hasinger G., 2007, *A&A*, 463, 79
 Gilli R., Comastri A., Vignali C., Ranalli P., Iwasawa K., 2010a, *X-ray Astronomy 2009; Present Status, Multi-Wavelength Approach and Future Perspectives*, 1248, 359
 Gilli R., Vignali C., Mignoli M., Iwasawa K., Comastri A., Zamorani G., 2010b, *A&A*, 519, A92
 Giustini M., Cappi M., Vignali C., 2008, *A&A*, 491, 425
 Granato G. L., Danese L., 1994, *MNRAS*, 268, 235
 Green P. J. et al., 1995, *ApJ*, 450, 51
 Hao H. et al., 2013, *MNRAS*, 434, 3104
 Häring N., Rix H., 2004, *ApJL*, 604, L89
 Hasinger G., 2008, *A&A*, 490, 905

- Hasinger G. et al., 2007, *ApJS*, 172, 29
- Hewett P. C., Foltz C. B., 2003, *AJ*, 125, 1784
- Hickox R. C., Mullaney J. R., Alexander D. M., Chen C.-T. J., Civano F. M., Goulding A. D., Hainline K. N., 2013, *ArXiv e-prints*. 1306.3218
- Hopkins P. F., Hernquist L., Cox T. J., Di Matteo T., Robertson B., Springel V., 2006, *ApJS*, 163, 1
- Ives J. C., Sanford P. W., Penston M. V., 1976, *ApJL*, 207, L159
- Iwasawa K. et al., 2012, *A&A*, 537, A86
- Iwasawa K., Taniguchi Y., 1993, *ApJL*, 413, L15
- Kaspi S., Maoz D., Netzer H., Peterson B. M., Vestergaard M., Jannuzi B. T., 2005, *ApJ*, 629, 61
- Kennicutt, Jr. R. C., 1998, *ARAA*, 36, 189
- Kishimoto M., Hönig S. F., Antonucci R., Barvainis R., Kotani T., Tristram K. R. W., Weigelt G., Levin K., 2011, *A&A*, 527, A121
- Kishimoto M., Hönig S. F., Beckert T., Weigelt G., 2007, *A&A*, 476, 713
- Koekemoer A. M. et al., 2007, *ApJS*, 172, 196
- Kolodzig A., Gilfanov M., Sunyaev R., Sazonov S., Brusa M., 2013, *A&A*, 558, A89
- La Franca F. et al., 2005, *ApJ*, 635, 864
- Lacy M., Petric A. O., Sajina A., Canalizo G., Storrie-Lombardi L. J., Armus L., Fadda D., Marleau F. R., 2007, *AJ*, 133, 186
- Lagos C. D. P., Padilla N. D., Strauss M. A., Cora S. A., Hao L., 2011, *MNRAS*, 414, 2148
- Lanzuisi G. et al., 2013, *MNRAS*, 431, 978
- Lawrence A., 1991, *MNRAS*, 252, 586
- Lawrence A., Elvis M., 1982, *ApJ*, 256, 410
- Lawrence A., Elvis M., 2010, *ApJ*, 714, 561
- Lilly S. J. et al., 2007, *ApJS*, 172, 70
- Lilly S. J. et al., 2009, *ApJS*, 184, 218
- Lusso E. et al., 2010, *A&A*, 512, A34
- Lusso E. et al., 2013, *ApJ*, 777, 86
- Lutz D. et al., 2011, *A&A*, 532, A90
- Mainieri V. et al., 2011, *A&A*, 535, A80
- Maiolino R. et al., 2007, *A&A*, 472, L33
- Maiolino R., Rieke G. H., 1995, *ApJ*, 454, 95
- Maiolino R. et al., 2010, *A&A*, 517, A47
- Malizia A., Bassani L., Bazzano A., Bird A. J., Masetti N., Panessa F., Stephen J. B., Ubertini P., 2012, *MNRAS*, 426, 1750
- Matt G., 2000, *A&A*, 355, L31
- Mayo J. H., Lawrence A., 2013, *MNRAS*, 434, 1593
- Menci N., Fiore F., Puccetti S., Cavaliere A., 2008, *ApJ*, 686, 219
- Merloni A. et al., 2010, *ApJ*, 708, 137
- Merloni A., Heinz S., 2013, in *Planets, Stars and Stellar Systems. Volume 6: Extragalactic Astronomy and Cosmology*, Oswald T. D., Keel W. C., eds., Springer Science+Business Media Dordrecht, p. 503
- Merloni A. et al., 2012, *MPE online publication*. *ArXiv e-prints*. 1209.3114
- Mignoli M. et al., 2013, *A&A*, 556, A29
- Mullaney J. R. et al., 2012, *MNRAS*, 419, 95
- Nandra K., Pounds K. A., 1994, *MNRAS*, 268, 405
- Nenkova M., Sirocky M. M., Nikutta R., Ivezić Ž., Elitzur M., 2008, *ApJ*, 685, 160
- Netzer H., 2008, *New Ast. Rev.*, 52, 257
- Netzer H., Laor A., 1993, *ApJL*, 404, L51
- Nicastro F., 2000, *ApJL*, 530, L65
- Panessa F., Bassani L., 2002, *A&A*, 394, 435
- Perola G. C. et al., 2004, *A&A*, 421, 491
- Pier E. A., Antonucci R., Hurt T., Kriss G., Krolik J., 1994, *ApJ*, 428, 124
- Poglitsch A. et al., 2010, *A&A*, 518, L2
- Predehl P., Schmitt J. H. M. M., 1995, *A&A*, 293, 889
- Richards G. T. et al., 2003, *AJ*, 126, 1131
- Richards G. T. et al., 2006, *ApJS*, 166, 470
- Risaliti G., Elvis M., Fabbiano G., Baldi A., Zezas A., Salvati M., 2007, *ApJL*, 659, L111
- Risaliti G., Elvis M., Nicastro F., 2002, *ApJ*, 571, 234
- Rosario D. J. et al., 2012, *A&A*, 545, A45
- Roseboom I. G., Lawrence A., Elvis M., Petty S., Shen Y., Hao H., 2013, *MNRAS*, 429, 1494
- Salvato M. et al., 2009, *ApJ*, 690, 1250
- Salvato M. et al., 2011, *ApJ*, 742, 61
- Sazonov S. et al., 2012, *ApJ*, 757, 181
- Scoville N. et al., 2007, *ApJS*, 172, 1
- Setti G., Woltjer L., 1989, *A&A*, 224, L21
- Shao L. et al., 2010, *A&A*, 518, L26
- Simpson C., 2005, *MNRAS*, 360, 565
- Steffen A. T., Barger A. J., Cowie L. L., Mushotzky R. F., Yang Y., 2003, *ApJL*, 596, L23
- Steffen A. T., Strateva I., Brandt W. N., Alexander D. M., Koekemoer A. M., Lehmer B. D., Schneider D. P., Vignali C., 2006, *AJ*, 131, 2826
- Tozzi P. et al., 2006, *A&A*, 451, 457
- Tran H. D., 2001, *ApJL*, 554, L19
- Tran H. D., 2003, *ApJ*, 583, 632
- Treister E., Krolik J. H., Dullemond C., 2008, *ApJ*, 679, 140
- Treister E., Urry C. M., 2006, *ApJL*, 652, L79
- Treister E. et al., 2006, *ApJ*, 640, 603
- Treister E., Urry C. M., Virani S., 2009, *ApJ*, 696, 110
- Tristram K. R. W. et al., 2009, *A&A*, 502, 67
- Trouille L., Barger A. J., Cowie L. L., Yang Y., Mushotzky R. F., 2009, *ApJ*, 703, 2160
- Trump J. R. et al., 2009, *ApJ*, 696, 1195
- Trump J. R. et al., 2007, *ApJS*, 172, 383
- Ueda Y., Akiyama M., Ohta K., Miyaji T., 2003, *ApJ*, 598, 886
- Urry C. M., Padovani P., 1995, *PASP*, 107, 803
- Vito F. et al., 2013, *MNRAS*, 428, 354
- Willott C. J., Rawlings S., Blundell K. M., Lacy M., 2000, *MNRAS*, 316, 449
- Winter L. M., Mushotzky R. F., Reynolds C. S., Tueller J., 2009, *ApJ*, 690, 1322
- Worsley M. A. et al., 2005, *MNRAS*, 357, 1281
- Young M., Elvis M., Risaliti G., 2009, *ApJS*, 183, 17

This paper has been typeset from a $\text{\TeX}/\text{\LaTeX}$ file prepared by the author.